# Study on Propagation of Atmospheric Gravity Waves in the Antarctic with Lidar Observation

木暮　優

博士（理学）

総合研究大学院大学
複合科学研究科
極域科学専攻

平成３０（２０１８）年度

# Study on Propagation of Atmospheric Gravity Waves in the Antarctic with Lidar Observation

Masaru Kogure

Department of Polar Science

School of Multidisciplinary Sciences

The Graduate University for Advanced Studies

March 2019

Abstract

Atmospheric gravity waves (AGWs) are generated in the lower atmosphere and they transport their energy and momentum into the upper atmosphere; this drives the circulation in the middle atmosphere. This effect of AGWs is usually described by parameterizations in practical general circulation models (GCMs), because AGWs are smaller than the grids of GCMs. However, AGW drag parameterization schemes do not represent their effects well, especially in the Antarctic, which results in a cold bias in the winter and spring stratosphere in the Antarctic. This cold bias leads to an underestimation of the ozone amount in winter and spring. Observations to quantify actual AGW characteristics are required to constrain the AGW drag parameterization scheme based on observations. In particular, the AGW drag over the Antarctic is underestimated, although the Antarctic region is well known as an AGW hot spot. This study investigated AGW activity with Rayleigh/Raman lidar (light detection and ranging) observations at Syowa Station (69° S, 40° E), which can observe temperature profiles in a wider altitude range than the typical lidar, i.e., Rayleigh lidar, to reveal the physical characteristics of Antarctic AGWs.

First, we derived the potential energy of AGWs per unit mass ($E_p$) in the altitude range of 15–70 km, indicating AGW activity, from the observed temperature profiles from May 2011 to October 2013, except for the summer periods. Four features of $E_p$ over Syowa were revealed: (1) The AGW activity was larger in winter than in spring and fall, except below the altitude of 30 km in 2012. This seasonal variation above 30 km is in good agreement with the results of previous studies using Rayleigh lidar at other Antarctic stations. (2) Above 30 km, $E_p$ values increased with a mean scale height of 11.3 km. This scale height is larger than the scale height at the Davis station ($69°$ S, $78°$ E) (~6.8 km), although both stations are located close to each other (~1500 km). (3) The local maxima of the $E_p$ profiles were near the altitude of 20 km and the local minima were near 25 km in almost all months, which has not been reported by previous studies. (4) The $E_p$ values in October 2012 are smaller at 35–60 km and larger at 20–35 km than those in October of 2011 and 2013, which could be caused by the critical level at which the zonal wind is weak (~35 km altitude). This result suggests that the critical-level filtering due to the weak zonal wind significantly influences the vertical and seasonal variation of $E_p$.

Subsequently, we derived $E_p$ for the following two years, i.e., 2014 and 2015, and found that the $E_p$ values between 50 and 60 km for August 8–21, 2014, except on August 12, were larger than the winter mean by more than one standard deviation. A ray-tracing analysis indicated the possibility that large-wavelength AGWs with the southwestward wavenumbers, emitted from various latitudes, converged near ~55 km over Syowa. This result suggests that the AGWs were refracted toward Syowa by the poleward tilting of the polar night jet (PNJ) with altitude. The AGW activity in the Antarctic middle atmosphere is enhanced by the horizontal propagation of the AGWs, which is not taken into account in practical GCMs. The PNJ condition on August 12 was similar to that during the enhancement, but the meridional wind at 0.5 hPa (~47 km altitude) changed drastically from +56 to −70 m/s during the observation period because of the passage of a synoptic-scale disturbance over Syowa. The decline in $E_p$ on August 12 could be caused by the critical-level filtering of AGWs due to the synoptic-scale disturbance. These results suggest that both the horizontal propagation and critical-level filtering strongly influence the day-to-day variations in AGW activity over Syowa.

This thesis implies that the local wind field controls Antarctic AGW activity in the middle

atmosphere through critical-level filtering. Additionally, the latitudinal structure of the zonal wind influences the AGW propagation path; this is a cause of local and temporal variation for the AGW activity, namely, intermittency.

Acknowledgements

The author thanks Drs. Takuji Nakamura (chief supervisor), Mitsumu K. Ejiri (co-supervisor), and Yoshihiro Tomikawa (co-supervisor during the time Dr. Ejiri spent at Syowa Station). Their dedicated instruction and support for the progress of the author's research and this Ph.D. thesis were invaluable. They instructed the author on Rayleigh/Raman lidar analysis methods and on reanalysis, presentations, and process of writing the research thesis. They also provided the author with many opportunities of discussion with eminent domestic and foreign researchers.

The author appreciates the useful instruction of and discussion with Drs. Masaki Tsutsumi and Takanori Nishiyama. Their expertise and knowledge regarding the middle atmosphere and their advice have helped the author immensely.

The author also appreciates Drs. Makoto Abo, Takuya D. Kawahara, Hidehiko Suzuki, and Takuo T. Tsuda. They developed the Rayleigh/Raman lidar and instructed the author on how to analyze the lidar data.

The author thanks the advisory committee member, Dr. Yasunobu Miyoshi, for his examination and evaluation of this Ph.D. thesis. His comments definitely improved this Ph.D. thesis.

The author thanks Dr. Damian J. Murphy of the Australian Antarctic Division. The valuable time which the author spent with him to discuss the propagation characteristics for atmospheric gravity waves improved Chapter 5 of this thesis significantly.

The author greatly thanks the members of the 52nd to 57th Japanese Antarctic Research Expeditions that operated the Rayleigh/Raman lidar at Syowa. The author also appreciates the Space and Upper Atmospheric Sciences Group staff of the National Institute of Polar Research for their kind support and encouragement in the five years of the author's Ph.D. work.

This thesis was partially supported by the Japan Society for the Promotion of Science (JSPS) Grant-in-Aid [JSPS Overseas Challenge Program for Young Researchers 201780038]

**Content**

# Chapter 1

## 1. General Introduction

### 1.1 Atmospheric Temperature and Wind Structures

The atmosphere is classified into four layers, the troposphere (0–10 km altitude), the stratosphere (10–50 km), the mesosphere (50–90 km), and the thermosphere (90–500 km), based on the vertical temperature structure in the atmosphere [e.g., *Holton*, 1992]. The vertical temperature structure is mainly determined by the distribution of the three major heat sources. The main heat source in the troposphere is the near-infrared absorption of water vapor. The mean temperature in the troposphere is maintained by the approximate balance among the near-infrared absorption of water vapor, the infrared radiative cooling of the atmosphere, and the vertical heat transport from the surface by eddies on several scales. Consequently, the tropospheric temperature decreases with altitude at a lapse rate of ~6 K $km^{-1}$. On the other hand, the temperature in the stratosphere increases with height because of the radiative balance between the infrared radiative cooling and the absorption of solar ultraviolet radiation by ozone. The boundary between the troposphere and stratosphere is called the tropopause (~10 km), where the atmospheric stability drastically changes (increases). The top of the stratosphere is called the stratopause (~50 km). The

temperature in the mesosphere decreases again up to ~90 km (the mesopause) because the absorption of solar ultraviolet radiation by ozone decreases with height. The atmospheric region including the stratosphere and the mesosphere is called the middle atmosphere. The temperature in the thermosphere increases with height because of the absorption of extreme ultraviolet radiation and ultraviolet radiation.

The meridional structure of temperature is quite different at each layer. Figures 1.1(a) and (b) show zonal mean temperature cross sections for January and July in the range of 0–120 km altitude from CIRA86 (COSPAR International Reference Atmosphere 1986) [*Fleming*, 1990]. The atmosphere from the surface to ~8 km has its latitudinal maximum temperature in the equatorial region, and the temperature decreases toward the winter and summer poles. The temperature in the upper troposphere and lower stratosphere has local minimums in the equatorial region and the winter polar region. In the middle and upper stratosphere, where ozone heating mainly determines the temperature structure, the maximum temperature is located in the summer pole, and the temperature decreases monotonically to the winter pole. On the other hand, the maximum temperature is located at the winter pole in the mesosphere. Such meridional structures in the middle atmosphere

are caused by diabatic heating due to radiation and adiabatic heating due to the pole-to-pole meridional circulation (① black arrows in Figures 1.1(a) and (b)), driven by atmospheric waves, as discussed in Section 1.2.

Figures 1.2(a) and (b) show the cross sections of the mean zonal wind for January and July for 0–120 km [*Fleming*, 1990]. The eastward wind is dominant in the troposphere of both hemispheres. The zonal wind has local maxima near the tropopause in the lower and middle latitudes. There is also a region of strong eastward wind in the middle atmosphere of the winter hemisphere, but the westward wind is dominant in the summer hemisphere. Such features are explained by the thermal wind balance, which is derived from the geostrophic balance and hydrostatic balance. The thermal wind balance is written as [*Holton*, 1992]

$$\frac{\partial u}{\partial z} = -\frac{g}{f}\frac{1}{T}\frac{\partial T}{\partial y}, \tag{1.1}$$

where $u$, $T$, $y$, and $z$ are zonal wind, temperature, northward location (positive north ward), and altitude, respectively. Parameters $g$ and $f$ are the gravitational acceleration and Coriolis parameter, respectively. This balance explains that the eastward (westward) component of the wind increases with altitude in a region in which the temperature

decreases (increases) from low (high) to high (low) latitudes. The temperature in the winter troposphere and stratosphere, except in the upper troposphere, increases from lower to higher latitudes such that the eastward wind increases with height in the winter hemisphere. The latitudinal gradient of temperature in the summer stratosphere is opposite to that in the summer troposphere, thus, the wind directions in each layer are opposite in the summer hemisphere. On the other hand, the temperature in the mesosphere and lower thermosphere increases from the summer to the winter poles; thus, the weak zonal wind layer is at the mesopause, and the wind direction in the thermosphere is opposite to that in the stratosphere. It should be noted that the thermal wind balance is a constraint but does not explain the causal relationship between the wind and temperature structures.

## 1.2 The Meridional Circulation in the Middle Atmosphere Driven by Atmospheric Waves

The meridional circulation in the stratosphere flows from equator to pole, while the meridional circulation in the mesosphere is a single cell flowing from the summer pole to the winter pole. The meridional components of these circulations are on the order of

1 m $s^{-1}$ or smaller, which is too slow to be observed directly. However, they strongly affect the transport and distribution of material, as well as temperature structures [*Butchart et al.*, 2011].

The stratospheric circulation, called the Brewer-Dobson circulation [*Dunkerton*, 1978; *Butchart et al.*, 2011], can be separated into deep and shallow branches (② and ③ black arrows in Figures 1.1(a) and (b)) [*Plumb*, 2002]. The deep branch is known to be the slower, weaker equator-to-pole circulation, which extends from the upper troposphere up to the upper stratosphere. The deep branch is driven by Rossby waves with a long wavelength ($\sim 2 \times 10^3 - \sim 4 \times 10^4$ km in the horizontal) and a long intrinsic period (longer than 1 day), and have westward phase speeds relative to the mean flow. The restoring force of such waves is the latitudinal gradient of the Coriolis parameter, i.e., $\beta$-effect. Rossby waves are generated in the troposphere by longitudinally dependent diabatic heating and orographic patterns, and then propagate vertically. Its influence in the middle atmosphere is preeminent in the winter hemisphere, because the stationary Rossby waves propagate only in the eastward wind. Finally, the Rossby waves deposit their westward momentum when they break. This deposition, i.e., the zonal drag force of

the Rossby wave decelerates the eastward jet, i.e., the polar night jet (PNJ). This drag force must be balanced by the Coriolis force in the meridional direction in a steady-state condition, which results in the deep branch of the Brewer-Dobson circulation [*Holton et al*., 1995]. The deep branch is present only in the winter hemisphere because the stationary Rossby waves can only propagate to the winter stratosphere. The shallow branch is driven by baroclinic waves, which have the same restoring force as Rossby waves (that is, $\beta$-effect). The waves have baroclinic instability structures (that is, the angle between surfaces of constant pressure and surfaces of constant density is large), with a smaller wavelength than that of Rossby waves. The mechanism of the shallow branch is the same as that of the deep branch, but the westward momentum is transposed in the lower stratosphere by the baroclinic waves. The shallow branch is the faster, stronger circulation from the equator to the pole in the lower stratosphere. This circulation is present in both hemispheres because of the presence of the baroclinic waves in the troposphere.

The meridional single-cell circulation in the mesosphere is driven by atmospheric gravity waves (AGWs), which have a short wavelength ($\sim 1 \times 10^1 - \sim 1 \times$

$10^3$ km in the horizontal) and short intrinsic period (shorter than the inertia period). The restoring force of AGW is the buoyancy force [*Leovy*, 1964; *Andrews et al.*, 1987; *Holton*, 1983; *Lindzen*, 1981]. Those waves propagate eastward (westward) relative to the mean flow, and they have eastward (westward) momenta. They transport their momenta into the middle atmosphere from the lower atmosphere through their vertical propagation. AGWs with eastward (westward) momentum can, however, most efficiently propagate in the summer (winter) hemisphere because of the eastward (westward) jet. This preference is caused by the critical level, which will be introduced in Chapter 2.1. This shows that the mean AGW drag forces cause flows in the mesosphere against the stratospheric jets. The mean AGW drag forces, such as the Rossby wave drag, should be balanced with the Coriolis force in the zonal direction, which leads to vertical flow via the mass conservation law. This vertical flow causes adiabatic heating/cooling, followed by a warm winter and cold summer mesopause.

In the last decade, it has been revealed that the AGW not only has an important role in mesospheric circulation but also in stratospheric circulation (i.e., Brewer-Dobson circulation). *Okamoto et al.* [2011] showed that AGWs also contribute to the Brewer-

Dobson circulation in the lower stratosphere over the lower and middle latitudes using reanalysis data and a Chemistry Climate Model. In particular, the upwelling part of the deep branch (low latitudinal parts of ② black arrows over the summer hemisphere in Figures 1.1(a) and (b)) is mainly caused by AGW drag, because the breaking of orographic AGWs tends to occur there on account of the weaker background wind. Recently, *Polichtchouk et al.* [2018] investigated the sensitivity of the Brewer-Dobson circulation and polar vortex to parameterized non-orographic AGW drag. They showed that variation in non-orographic AGW drag leads to variation in the Rossby and baroclinic wave drag. Thus, AGW not only drives the global circulation but also influences Rossby and baroclinic waves.

To summarize, Rossby waves, baroclinic waves, and AGWs drive the meridional circulation and change the temperature structure in the middle atmosphere. Furthermore, these types of waves also interact with each other, causing uncertainty in the prediction of long-term climate trends.

# Chapter 2

## 2. Atmospheric Gravity Wave (AGW)

### 2.1 Characteristics of the AGW

As mentioned in the previous chapter, AGWs transport their momentum vertically, driving the meridional circulation in the middle atmosphere.

Here, the characteristics of AGWs, particularly their vertical propagation, are introduced based on AGW linear theory [e.g., *Holton*, 1992; *Fritts and Alexander*, 2003], and the propagation and activity of AGWs are investigated in this study. The fluid equations in the Earth's atmosphere are described as follows,

$$\frac{\mathrm{D}u}{\mathrm{D}t} - fv + \frac{1}{\rho}\frac{\partial P}{\partial x} = 0 \tag{2.1}$$

$$\frac{\mathrm{D}v}{\mathrm{D}t} + fu + \frac{1}{\rho}\frac{\partial P}{\partial y} = 0 \tag{2.2}$$

$$\frac{Dw}{Dt} + \frac{1}{\rho}\frac{\partial P}{\partial z} + g = 0 \tag{2.3}$$

$$\frac{1}{\rho}\frac{D\rho}{Dt} + \frac{\partial u}{\partial x} + \frac{\partial v}{\partial y} + \frac{\partial w}{\partial z} = 0 \tag{2.4}$$

$$\frac{D\theta}{Dt} = 0 \tag{2.5}$$

$$\theta = \frac{P}{\rho R}\left(\frac{P_0}{P}\right)^{\frac{R}{C_p}} \tag{2.6}$$

where $x$, $y$, and $z$ represent location ($x$: positive eastward, $y$: positive northward, and

*z*: positive upward); *u*, *v*, and *w* are the zonal, meridional, and vertical wind velocities, respectively; and *P* and $\rho$ are the pressure and mass density, respectively. Parameters $g$, *f*, $\theta$, *R*, and $C_p$ are the gravitational acceleration, Coriolis parameter, potential temperature, gas constant, and dry air specific heat at constant pressure, respectively. The adiabatic process is assumed, and nonconservative terms are neglected in Eqs. (2.1)–(2.6). Assuming a horizontally uniform background state and linearizing the parameters, the following equations are obtained,

$$\frac{\mathrm{D}u'}{\mathrm{Dt}} - fv' + \frac{\partial}{\partial x}\frac{P'}{\rho_0} = 0 \tag{2.7}$$

$$\frac{\mathrm{D}v'}{\mathrm{Dt}} + fu' + \frac{\partial}{\partial y}\frac{P'}{\rho_0} = 0 \tag{2.8}$$

$$\frac{Dw'}{Dt} + \frac{\partial}{\partial z}\frac{P'}{\rho_0} - \frac{1}{H}\frac{P'}{\rho_0} + g\frac{P'}{\rho_0} = 0 \tag{2.9}$$

$$\frac{D}{Dt}\frac{\rho'}{\rho_0} + \frac{\partial u'}{\partial x} + \frac{\partial v'}{\partial y} + \frac{\partial w'}{\partial z} - \frac{w'}{H} = 0 \tag{2.10}$$

$$\frac{\mathrm{D}}{\mathrm{D}t}\frac{\theta'}{\theta_0} + \mathrm{w}'\frac{N^2}{g} = 0 \tag{2.11}$$

$$\frac{\theta'}{\theta_0} = \frac{1}{c_s^2}\frac{P'}{\rho_0} - \frac{P'}{\rho_0} \tag{2.12}$$

where the primes (′ ) indicate perturbations due to the AGW, and the subscripts of “0” indicate the background states, which satisfy the hydrostatic balance, $\frac{\partial P_0}{\partial z} = -\rho_0 g$. $N(z)$ is the Brunt–Väisälä frequency, derived as

$$N_{(z)}^2 = \frac{g}{\overline{T}_{0(z,t)}}\left[\frac{d\overline{T}_{0(z,t)}}{dz} + \frac{g}{C_p}\right]. \quad (2.13)$$

$H$, $T$, and $c_s$ are the density scale height, temperature, and speed of sound, respectively. The bar indicates a time-averaged quantity. The background horizontal wind shear and second-order terms are neglected. Now, we assume three conditions: (1) $N$ varies slowly in one wave cycle in the vertical ( i.e., the WKB approximation). (2) The speed of sound ($c_s$) is significantly larger than the phase speed of the AGW($c$) (i.e., the Boussinesq approximation). (3) The solutions of (2.7)–(2.12) are in the form of a planar wave. The condition of (3) is expressed as:

$$\left(u', v', w', \frac{\theta'}{\theta_0}, \frac{P'}{\rho_0}, \frac{\rho'}{\rho_0}\right) = \left(\tilde{u}, \tilde{v}, \tilde{w}, \tilde{\theta}, \tilde{P}, \tilde{\rho}\right) \cdot \exp\left[i(kx + ly + mz - \hat{\omega}t) + \frac{z}{2H}\right]. \quad (2.14)$$

Here, terms with tildes indicate the amplitudes of those parameters.

Assuming the second condition ($c_s \gg c$), the dispersion relation equation of the AGW is acquired as follows,

$$m^2 = \frac{(k^2 + l^2)(N^2 - \hat{\omega}^2)}{(\hat{\omega}^2 - f^2)} - \frac{1}{4H^2} \quad (2.15)$$

where *m*, *k*, and *l* are the vertical, zonal, and meridional wavenumbers, respectively, and $\hat{\omega}$ is the intrinsic frequency, i.e., the frequency of the AGW relative to the background flow.

The dispersion relationship determines the AGW characteristics (e.g., wavenumber and intrinsic frequency). The intrinsic frequency, $\hat{\omega}$, is described as

$$\hat{\omega} = \omega - ku_0 - lv_0. \tag{2.16}$$

where $\omega$ is the ground-based frequency, i.e., the frequency of the AGW relative to the ground. Most observation instruments observe $\omega$ instead of $\hat{\omega}$. It should be noted that the vertical component of the background wind, $w_0$, is neglected in Eq. (2.16) because of the assumption of hydrostatic balance. The AGW group velocity, $\boldsymbol{c_g}$, is the velocity of the envelope of a wave packet, which can be expressed as:

$$\begin{aligned} \boldsymbol{c_g} &= \left(c_{gx}, c_{gy}, c_{gz}\right) = \left(\frac{\partial\omega}{\partial k}, \frac{\partial\omega}{\partial l}, \frac{\partial\omega}{\partial m}\right) \\ &= (u_0, v_0, 0) + \frac{[k(N^2 - \hat{\omega}^2),\ l(N^2 - \hat{\omega}^2), -m(\hat{\omega}^2 - f^2)]}{\hat{\omega}\left(k^2 + l^2 + m^2 + \frac{1}{4H^2}\right)}. \end{aligned} \tag{2.17}$$

Here, we define $\hat{\omega} \geq 0$, and $m$ is negative (positive) for upward (downward) group velocity. The source location and propagation path of the AGW can be investigated using Eq. (2.17). When the AGW propagates vertically and then approaches the altitude where $m^2 \rightarrow \infty$ (i.e., $\hat{\omega}^2 \rightarrow f^2$), the AGW cannot reach that altitude within a finite time; that is, the AGW cannot cross that altitude. This altitude is called the critical level. The critical level strongly affects the propagation of AGWs and the vertical distribution of AGW

activity, which are discussed in chapters 4 and 5. On the other hand, when the wave encounters the altitude where $m^2 \to 0$, the sign of its vertical group velocity changes, and the vertical propagation direction is reversed. Such an altitude is called a turning level. Critical and turning levels are important concepts in understanding how AGWs propagate in the middle atmosphere. Besides these concepts, the refraction of the AGW, caused by the horizontal wind shear, is also an important factor. Refraction affects the propagation of the wave and causes high AGW activity around the PNJ [*Dunkerton*, 1984; *Sato et al.*, 2009; *Alexander et al.*, 2016]. The wavenumber vector is changed by the refraction, and its time rate of change is described as follows,

$$\frac{\mathrm{d}k}{\mathrm{d}t} = -\left(k\frac{\partial u_0}{\partial x} + l\frac{\partial v_0}{\partial x}\right) \tag{2.18}$$

$$\frac{\mathrm{d}l}{\mathrm{d}t} = -\left(k\frac{\partial u_0}{\partial y} + l\frac{\partial v_0}{\partial y} + \frac{\beta f}{\widehat{\omega}}\right) \tag{2.19}$$

where $\beta = \frac{\mathrm{d}f}{\mathrm{d}y}$ is the Rossby parameter and $\frac{\mathrm{d}}{\mathrm{dt}}$ indicates the time rate of change of the parameter it is applied to. It should be noted that the third term on the right hand of (2.19) is an effect of the spherical coordinate system. Magnitude $\left|\frac{dl}{dt}\right|$ is typically larger than $\left|\frac{dk}{dt}\right|$, especially around the PNJ, because the meridional gradient of the zonal wind, $\frac{\partial u_0}{\partial y}$, is larger than the other gradient terms.

Finally, the wave energy, which is a measure of AGW activity, is introduced. The wave energy per unit mass, $E$, is defined as [*Whiteway and Carswell*, 1994]

$$E = E_p + E_k = \frac{1}{2}\left(\frac{g}{N}\right)^2 \overline{\left(\frac{\rho'}{\rho_0}\right)^2}^e + \frac{1}{2}\left(\overline{u'^2}^e + \overline{v'^2}^e + \overline{w'^2}^e\right) \tag{2.20}$$

where the bars ($\bar{}^e$) indicate the ensemble average, and $E_k$ is called the kinetic energy of the AGW per unit mass, which is related to the wind perturbations. Meanwhile, $E_p$ is called the potential energy of the AGW per unit mass, which is related to the relative density perturbation. $E_p$ is rewritten under the Boussinesq approximation as

$$E_p = \frac{1}{2}\left(\frac{g}{N}\right)^2 \overline{\left(\frac{\rho'}{\rho_0}\right)^2}^e = \frac{1}{2}\left(\frac{g}{N}\right)^2 \overline{\left(\frac{T'}{T_0}\right)^2}^e \tag{2.21}$$

where $T$ is the temperature. In this study, $E_p$ is investigated from the temperature obtained by Rayleigh/Raman (RR) lidar.

## 2.2 Current Understanding of the AGW in Antarctica and the Purpose of This Study

AGWs have been studied for several decades not only to understand atmospheric circulation and vertical coupling but also to improve general circulation models (GCMs). As mentioned previously, the AGW drives the atmospheric circulation, but current operational GCMs cannot explicitly represent the full spectrum of AGWs because of limitations of computational resources. To treat its effect on GCMs, parameterizations are usually implemented. The parameterizations are generally grouped, based on the AGW source, into two categories: (1) orographic AGW drag schemes, which represent the AGW drag generated from the flow over subgrid-scale topography, and (2) non-orographic AGW drag schemes, which represent the AGW drag generated by generation mechanisms other than topography. The orographic AGW drag scheme is more reliable than the non-orographic scheme because the orographic generation mechanisms are better quantitatively understood. The practical parameterizations apply several kinds of assumptions to decrease computation costs. For example, the practical schemes assume two points: (1) The AGW propagates only upward, and (2) the AGW conserves its energy

and momentum up to its critical level or a height, where the amplitude of the AGW is saturated. The parameters of the AGW in the parameterization scheme (e.g., its period, horizontal wavelength, and amplitude) can be tuned to reproduce realistic zonal wind fields. However, several studies have demonstrated the difficulty in correctly representing AGWs with AGW drag parameterizations, degrading the reproducibility of GCMs because of the complex nature of AGWs [*Alexander et al.*, 2010; *Bühler and McIntyre*, 2003; *Geller et al.*, 2013; *Hertzog et al.*, 2012]. They have also mentioned that the AGW parameters should be physically constrained based on observations, but the current physical knowledge about AGWs is not sufficient. Thus, observations to quantify actual AGW parameters are required to understand the behavior of AGWs.

The observations of the AGW in the troposphere and the middle atmosphere have been performed by several kinds of in-situ (e.g., radiosondes) and ground-based instruments (e.g., lidar and radar). Here, the commonly-used atmospheric lidar (that is, Rayleigh lidar) studies are introduced as this thesis considers Rayleigh/Raman lidar. Rayleigh lidar can observe the density and temperature (an observation technique of Rayleigh lidar is described in Chapter 3). It can observe the altitude region from the middle

stratosphere to the lower mesosphere, which is hardly covered by in-situ observations and radar. *Chanin and Hauchecorne* [1981] is the first study to report AGW density perturbation profiles with Rayleigh lidar at Haute-Provence (44° N, 6° E) over several nights. Some studies [e.g., *Gardner et al.*, 1989; *Shibata et al.*, 1986] also observed AGWs in the middle latitude of the northern hemisphere. Ten years after the *Chanin and Hauchecorne* study, *Wilson et al.* [1991] showed the seasonal variation of AGW activity with Rayleigh lidar (Figure 2.1). They reported that the AGW activity has a seasonal cycle with a maximum in winter and minimum in summer at Haute-Provence. Other studies [e.g., *Whiteway and Carswell*, 1995] observed the AGW with the Rayleigh lidar and showed the same seasonal cycle in the middle latitude of both hemispheres and Arctic regions. This seasonal cycle is caused by critical-level filtering [*Fritts and Alexander*, 2003]. Several studies [e.g., *Sivakumar et al.*, 2006; *Li et al.*, 2010] observed AGWs with Rayleigh lidar in the equatorial regions, and they suggested that the equatorial AGW activity was strongly affected by the semiannual oscillation and quasi-biennial oscillation. In the Antarctic region, Rayleigh lidar observations have been conducted at Rothera [*Yamashita et al.*, 2009], the South Pole [*Yamashita et al.*,

2009], McMurdo [*Liu et al.*, 2014; *Zhao et al.*, 2017; *Chu et al.*, 2018], and Davis [*Alexander et al.*, 2011; *Kaifler et al.*, 2015]. These reports suggest that AGW activity has the same seasonal cycle in Antarctica as those in the middle latitudes and Arctic (i.e., maximum in winter and minimum in summer) (Figure 2.2), except that at the South Pole, which does not have a clear seasonal cycle.

Ground-based and in-situ instruments have revealed in detail the temporal variation of AGW activity at several sites, but they hardly revealed the AGW activity over the ocean or places that lack much human activity. Some satellite instruments can observe the temperature in the middle atmosphere and provide a global map of AGW activity with long horizontal wavelengths (i.e., ≥ 200–300 km), which has helped us to understand the relationship among the AGW activity, background meteorological fields, and topography [*Tsuda et al.*, 2000; *Tsuda and Hocke*, 2004; *Baumgaertner and McDonald*, 2007; *Alexander et al.*, 2009; *Ern et al.*, 2011; *Liu et al.*, 2014]. *Ern et al.* [2011] showed latitudinal variations of the zonal mean absolute momentum flux of AGW observed by three satellite instruments, i.e., Cryogenic Infrared Spectrometers and Telescopes for the Atmosphere (CRISTA) on the CRISTA-Atmosphere Shuttle Palette

Satellite (CRISTA-SPAS) in August 1998, High Resolution Dynamics Limb Sounder (HIRDLS) on Aura, and Sounding of the Atmosphere using Broadband Emission Radiometry (SABER) on the Thermosphere Ionosphere Mesosphere Energetics and Dynamics (TIMED) spacecraft in August 2006 (Figure 2.3). They showed that the absolute momentum flux in the middle atmosphere has a maximum at 60° S, which suggests that this area is an AGW hot spot in austral winter. *Geller et al.* [2013] also found the peak of the absolute momentum flux in ~ 60° S from the temperature observations by HIRDLS and SABER in July 2006. Thus, the satellite observations have revealed that the higher latitudes in southern hemisphere is one of the AGW hot spots.

Both AGW-resolving GCMs and GCMs containing AGW parameterization schemes have showed latitudinal variations in the absolute momentum flux qualitatively similar to those demonstrated by satellite observations [*Sato et al.*, 2012; *Geller et al.*, 2013]. However, *Geller et al.* [2013] pointed out that the magnitudes of the absolute momentum flux in the stratosphere over the Antarctic were quite variable among the GCMs. In addition, *Garcia et al.* [2017] pointed out that the amplitudes of the AGWs

over Antarctica were underestimated by the parameterization scheme, which caused an overestimation of ozone depletion. *Butchart et al*. [2011] also showed that inaccurate representations of AGW drag lead to a cold bias and overestimation of ozone depletion in the GCMs. Although there are several possibilities for inaccurate representations of AGW drag, particularly in the Antarctic region, we introduce two possibilities.

One possibility is inaccurately represented sources of AGW. The sources are classified as orographic and non-orographic sources. *Hoffmann et al.* [2013] reported that not only the two main hot-spot areas (i.e., the Antarctic Peninsula and the southern Andes) but also islands (i.e., subgrid-scale topography in the southern oceans) often generate orographic AGWs. The lack of AGWs generated by such a small-scale topography in the parameterization scheme could lead to the inaccurate representation of AGW drag [*Alexander et al.*, 2010; *Garcia et al.*, 2017]. Non-orographic AGWs are generated by mechanisms other than orography (e.g., convection, instability, and flow imbalance). The generation mechanisms of non-orographic AGWs are not yet well understood, and knowledge regarding the parameters of generated AGWs are insufficient, which could lead to the inaccurate representation of AGW drag [*Plougonven and Zhang*, 2014]. One

of the major sources of the non-orographic AGW in Antarctica is the spontaneous adjustment caused by the flow imbalance of the PNJ. *Sato and Yoshiki* [2008] observed the large-amplitude AGWs in the lower stratosphere at Syowa (69° S, 40° E) using radiosonde observations (Figures 2.4a and b). They showed that the imbalance of the lower stratospheric PNJ was enhanced around Syowa (Figures 2.4c and d) and generated AGWs. Another major source of non-orographic AGWs is the tropospheric baroclinic wave. *Hendricks et al.* [2014] found a high correlation between the lower stratospheric AGW activity and the maximum eddy growth rate, which is used as a proxy for baroclinic wave activity, in the middle troposphere during austral winter.

The other possibility for the inaccurate representation of AGW drag is the neglect the horizontal propagation of AGWs. Most of the AGW drag parameterization schemes in the practical GCMs assume that AGWs propagate only in the vertical direction. However, several studies [*Alexander et al.*, 2016; *Dunkerton*, 1984; *Sato et al.*, 2009] demonstrated that AGWs can propagate over long horizontal distances (i.e., ≥ 1000 km). These studies showed that horizontal propagation caused an increase in AGW activity around the PNJ, because the AGWs were refracted to the PNJ and converged to

that region. *Kalisch et al.* [2014] showed that neglecting horizontal propagation provides a significant bias in the magnitude and direction of the AGW drag using global AGW ray-tracing simulations, but there are many observations that serve as evidence. The purpose of this study is to reveal the propagations, sources, and characteristics of AGW over the Antarctic, using Syowa Rayleigh/Raman lidar observations. We focus on two points: (1) The relationship between AGWs and the background wind condition, and (2) the causes of the temporal, vertical, and horizontal variation in AGW activity (i.e., intermittency).

# Chapter 3

## 3. Rayleigh/Raman Lidar Observation and Analysis

An atmospheric lidar emits laser pulses into the atmosphere and detects backscattered signals. Lidar can measure atmospheric temperature, atmospheric density, wind, aerosol, clouds, and density of trace gases from their backscattered signals. Many atmospheric studies have involved the observation of AGWs with lidar [e.g., *Whiteway and Carswell*, 1994, *Duck et al.*, 2001, *Kaifler et al.*, 2015, *Baumgarten et al.*, 2015]. This thesis investigates the AGW activity from the temperature profiles with a Rayleigh/Raman (RR) lidar instrument at Syowa (Figure 3.1). In this section, the RR lidar observation system and our analysis are introduced.

An RR lidar instrument, used to profile the atmospheric temperature between the altitudes of 10 and 80 km, was installed in January 2011 at Syowa Station, the Antarctic (69° S, 40° E) by the 52nd Japanese Antarctic Research Expedition (JARE52). The main transmitter is a pulsed Nd:YAG laser (355 nm) with a 300-mJ pulse energy and a 20-Hz repetition frequency. The receiver telescope has a primary mirror with a diameter of 82 cm and is equipped with three photomultiplier tubes (PMTs). Two PMT channels, the

Rayleigh high and low channels, are used to detect the Rayleigh backscattered signal, at 355 nm, from high (23–90 km) and low (10–70 km) altitudes. The other PMT channel, the Raman channel, is used to detect the $N_2$ vibrational Raman backscattered signal at 387 nm, between 10 and 40 km. This Raman channel enabled the RR lidar to cover the lower stratosphere for which the typical Rayleigh lidar cannot obtain the temperature. The height and time resolutions of photon counts observed by the RR lidar are 7.5 or 15 m, and 1 min (1200 shots), respectively (Figure 3.2). Further details and validations of the RR lidar system are described by *Suzuki et al.* [2012]. In this study, the observed photon counts were integrated over a vertical range of 0.9 km and a period of 1 h to reduce the random errors caused by shot noise. The temperature profiles were then calculated between the altitudes of 10 and 80 km, excluding the summer periods. In Chapter 4, data between May 2011 and October 2013 are used. In Chapter 5, two more years of data in 2014 and 2015 are added and analyzed.

### 3.1 Rayleigh Integration Method

This thesis used the Rayleigh integration method introduced by *Hauchecorne and Chanin* [1980] to obtain the temperature. In this section, we will introduce the Rayleigh

integration method, which provides the temperature profile from the Rayleigh ($N_2$ vibration Raman) backscattered signal profile.

The lidar equation describes the relationship between the backscattered signal, $Si(z_i)$, and the atmospheric density, $\rho(z_i)$, in the i[th] altitude layer [*Hauchecorne and Chanin*, 1980],

$$Si(z_i) = \frac{AO(z_i)T_{r_1}(z_0, z_i)T_{r_2}(z_0, z_i)}{(z_i - z_0)^2}(\rho(z_i)b + B_{mie})\Delta z \qquad (3.1)$$

where the instrument factor of the lidar system, $A$, is constant, $O(z_i)$ is the instrumental overlap function and is considered to be constant above 10 km in this study, $T_{r_1}(z_0, z_i)$ and $T_{r_2}(z_0, z_i)$ are the atmospheric transmittance between $z_i$ and $z_0$ (the bottom altitude of the investigated profile, i.e., 10 km). Parameter $\Delta z$ is the thickness of the i[th] altitude layer, $b$ is the Rayleigh (the $N_2$ vibration Raman) backscattering cross-section, and $B_{mie}$ is the Mie backscattering coefficient. The Mie backscatter signal is of the same wavelength as the Rayleigh backscatter, thus, it is difficult to separate both signals. The aerosol density is significantly small above the middle stratosphere, and the Mie backscattered signal can be neglected. The Raman backscattered signal has a different wavelength from the Mie one, so that the Raman backscattered signal is not affected by

the Mie backscattered signal.

The combination of the gas law and the hydrostatic equilibrium equation leads to

$$T(z_i) = \frac{g\Delta z}{Rln\left[\frac{P\left(z_i - \frac{\Delta z}{2}\right)}{P\left(z_i + \frac{\Delta z}{2}\right)}\right]}. \quad (3.2)$$

From the hydrostatic equilibrium equation, $P\left(z_i - \frac{\Delta z}{2}\right)$ and $P\left(z_i + \frac{\Delta z}{2}\right)$ are described as

$$P\left(z_i + \frac{\Delta z}{2}\right) = \Sigma_{j=i+1}^{N}\rho(z_j)g\Delta z + P(z_N + \frac{\Delta z}{2}) \quad (3.3)$$

$$P\left(z_i - \frac{\Delta z}{2}\right) = \rho(z_i)g\Delta z + P\left(z_i + \frac{\Delta z}{2}\right). \quad (3.4)$$

Parameter $z_N$ is the top altitude in which the lidar can measure the backscattered signal. Thus, the density profile can be acquired from (3.1), with which (3.3) and (3.4) yield the pressure profile. The reference value of $P(z_N + \frac{\Delta z}{2})$ is acquired from the CIRA86 model [*Fleming et al.*, 1990] in this study to solve (3.4), which can be used to obtain the temperature profile from (3.2).

To acquire $T_{r_1}(z_0, z_i)$ and $T_{r_2}(z_0, z_i)$, the atmospheric extinction coefficient over Syowa is calculated for altitudes between 10 and 90 km. The extinction coefficient profile in an altitude range of 20–90 km is calculated based on the method introduced by

*Hauchecorne and Chanin* [1980]. Namely, the extinction coefficient profiles are estimated using atmospheric Rayleigh scattered extinction, because Mie scattered extinction is significantly small. The atmospheric density is obtained from radiosonde observations up to the top height of observation. Then, CIRA86 (COSPAR International Reference Atmosphere) [*Fleming et al.*, 1990] is used from the top of the radiosonde observation height and 90 km altitude. The Rayleigh scattered extinction coefficient is calculated as described in *Bucholtz* [1995]. To determine the photon count profiles of the Rayleigh low channel, assuming that the Mie backscattered signal and extinction can be neglected, the extinction profiles between the altitudes of 10 and 20 km are calculated using the same method as used above the 20-km altitude. The assumption is probably unsatisfactory for use in the lower altitude. On the other hand, the extinction profile for the photon count profile of the Raman channel between the altitudes of 10 and 20 km is determined by the total extinction coefficient, which includes the Mie scattered extinction, because the Mie scattered extinction in the lower stratosphere cannot be typically neglected.

The total extinction for analyzing the Raman channel between 10 and 20 km is calculated

based on the method introduced by *Ansmann et al.* [1990] to examine the total extinction profile in that region. The total round-trip extinction coefficient, $\alpha_{total}(z)$, is written as

$$\alpha_{total}(z) = \alpha_{355}(z) + \alpha_{387}(z) = \frac{d}{dz}\ln\left(\frac{O(z)\rho(z)}{z^2 Si(z)}\right), \qquad (3.5)$$

where $\alpha_{355}(z)$ and $\alpha_{387}(z)$ are the total extinction coefficients at the wavelengths of 355 nm and 387 nm, respectively. Parameter $\rho(\mathrm{z})$ is the atmospheric density obtained from the radiosonde observation acquired at 0 UT, and $Si(\mathrm{z})$ is the Raman signal at the 387-nm wavelength between 23:30–00:30 UT. Assuming that the ratio of the Mie extinction to the atmospheric molecular extinction is constant between the altitudes of 10 and 20 km, $\ln\left(\frac{O(z)\rho(z)}{z^2 Si(z)}\right)$ must be a linear function of $z$. On that assumption, $\alpha_{total}(z)$ is derived by a linear least squares fitting. The total extinction coefficient profile between the altitudes of 10 and 20 km can be determined from $\alpha_{total}(z)$, and the atmospheric density is obtained by the radiosonde observation. The difference between the temperature profiles obtained by the radiosonde observation and the Raman channel using the total extinction profile introduced here is smaller than 1 K between the altitudes of 10 and 20 km, though the temperature obtained by the Raman channel, neglecting Mie extinction, is ~3 K colder around 15 km and ~6 K colder around 10 km than the

radiosonde observations, on average. The extinction coefficient $\alpha_{total}(z)$ is applied to all Raman signal profiles during the night, assuming that the time variation of the total extinction between altitudes of 10 and 20 km is significantly small during the night.

Examples of the three temperature profiles obtained using the three receiver channels are shown in Figure 3.3(a). The top altitude, $z_N$, is given at the highest altitude at which the relative error of the backscattered signal caused by shot noise does not exceed 20% (typically ~90 km altitude for the Rayleigh high channel, ~70 km altitude for the Rayleigh low channel, and ~40 km altitude for the Raman channel). The reference pressure value, $P\left(z_N + \frac{\Delta z}{2}\right)$, is acquired from the density observed by the RR lidar and a reference temperature value taken from CIRA86 [*Fleming et al.*, 1990] for the Rayleigh high channel. On the other hand, temperatures derived from the Rayleigh high and low channels are used as the reference temperature values for the Rayleigh low and Raman channels, respectively. The temperature profiles obtained from the three observation channels are then merged into one profile, $T(z, t)$, and that profile is used for the investigation of AGW activity. The details of how to merge the three profiles are described later.

Finally, the statistical error of the temperature measurement, $\delta T(z_i)$, is calculated as follows. The relative temperature error is described in *Hauchecorne and Chanin* [1980],

$$\frac{\delta T(z_i)}{T(z_i)} = \frac{\delta X(z_i)}{(1 + X(z_i))\ln|1 + X(z_i)|} \tag{3.6}$$

where $X$ is defined as

$$X(z_i) = \frac{\rho(z_i) g \Delta z}{P\left(z_i + \frac{\Delta z}{2}\right)}. \tag{3.7}$$

Parameter $\delta X(z_i)$ is composed of two factors, $\delta\rho(z_i)$ and $\delta P\left(z_i + \frac{\Delta z}{2}\right)$, and is expressed as

$$\left(\frac{\delta X(z_i)}{X(z_i)}\right)^2 = \left(\frac{\delta\rho(z_i)}{\rho(z_i)}\right)^2 + \left(\frac{\delta P\left(z_i + \frac{\Delta z}{2}\right)}{P\left(z_i + \frac{\Delta z}{2}\right)}\right)^2. \tag{3.8}$$

The second term includes two types of errors from the real value in the atmosphere. One is caused by the difference in the reference pressure $P\left(z_N + \frac{\Delta z}{2}\right)$, and the other is caused by the photon-counting noise (i.e., shot noise) between $z_N$ and $z_i + \frac{\Delta z}{2}$. However, the second term in Eq. (3.8) becomes negligible at altitudes sufficiently lower than $z_N$, e.g., at 10 km lower than $z_N$. Thus, (3.6) can be rewritten as

$$\frac{\delta T(z_i)}{T(z_i)} = \frac{\delta\rho(z_i)}{(1 + X(z_i))\ln|1 + X(z_i)|} \frac{g\Delta z}{P\left(z_i + \frac{\Delta z}{2}\right)}. \tag{3.9}$$

Parameter $\delta\rho(z_i)$ is estimated from the shot noise at $z_i$, and $\delta T(z_i)$ is calculated from (3.8). The typical temperature error standard deviation is 6 K at 80 km and is no larger

than 1 K below 60 km.

Figure 3.3(b) shows the merged temperature profile, $T(z, t)$, acquired at 00 UT on June 27, 2012. Figure 3.3(b) also shows the temperature profile observed by a radiosonde at the same time as the RR lidar. The two temperature profiles agree well. $T(z, t)$ above the 40-km altitude is observed by the Rayleigh high channel. At altitudes between 25 and 40 km, the temperatures derived from the Rayleigh high and low channels are averaged using a weighting of the inverse of the square of the standard deviation of the temperature. Subsequently, from 25 km to the "merging altitude," $T(z, t)$, derived by the Rayleigh low channel, is used. The merging altitude is selected to be between 10 and 20 km, thus, the mean square of the temperature difference between the Rayleigh low and Raman channels in the 2.7-km height range is minimized. At the merging altitude and two adjacent heights (above and below), $T(z, t)$ is given as an averaged temperature between the Rayleigh low and Raman channels. Between the merging altitude and 10 km, the Raman channel is used. In Figure 3.3(b), the merging altitude was selected to be 19.35 km. Note that in the presence of polar stratospheric clouds (PSCs) with a backscatter ratio (BSR) larger than 1.05, the merging altitude is selected to be above the top of the PSCs. The BSR was

calculated from the ratio of the signal intensities of the Rayleigh low and Raman channels [*Ansmann et al.*, 1992].

### 3.2 Potential Energy of the AGW ($E_p$)

As described in Chapter 2, the potential energy of the AGW per unit mass, $E_p(z)$, is proportional to the square of the relative temperature perturbation of the AGW and indicates AGW activity.

The temperature perturbation, *T'*(*z*, *t*), is calculated as

$$T'(z,t) = T(z,t) - T_0(z,t), \qquad (3.1)$$

where $T_0(z,t)$ is the background temperature profile. $T_0(z,t)$ is derived from each temperature profile, *T*(*z*, *t*), at time *t*, based on a method introduced by *Duck et al.* [2001] and *Ehard et al.* [2015]. In a window with a 24-km altitude range, the temperature profile is fitted by a cubic polynomial function. Subsequently, the window is shifted by a 0.9 km step to obtain the fitted profiles. The fitted temperature values at each height are averaged, with an emphasis on the central 8 km in the profile fittings. Details of the weighting function are found in *Duck et al.* [2001]. Finally, the weighted average profile is smoothed by applying a 5.4-km running average. Further details of this method are described by

*Duck et al.* [2001]. Note that the above process extracts the temperature perturbations of AGWs with vertical wavelengths ($\lambda_z$) of 1.8–16 km. It is also noteworthy that AGWs with periods ($\tau$) longer than 2 h (the Nyquist period) were extracted as well. Examples of two temperature profiles, $T(z,t)$ and $T_0(z,t)$, acquired at 00 UT on June 27, 2012, are shown in Figure 3.3(b), and the resultant $T'(z,t)$ profiles are plotted in Figure 3.3(c). The term $\frac{d\overline{T_0(z,t)}}{dz}$ is calculated using a linear least squares fit over a 10-km height range, and the time average is assumed to be nightly mean. The vertical Fourier components of $T'(z,t)$ and its Hilbert transform, $T_h'(z,t)$, have the same amplitude and are out of phase by 90° [*Bracewell*, 1999]:

$$\overline{T'^2(z,t)} = \overline{T_h'^2(z,t)}. \tag{3.2}$$

Thus, $E_p(z)$ is also written as

$$E_p(z) = \frac{1}{2}\left(\frac{g}{N(z)}\right)^2 \left[\frac{1}{2}\left(\frac{\overline{T'^2(z,t) + T_h'^2(z,t)}}{T_0^2(z,t)}\right)\right]. \tag{3.3}$$

$T_h'(z,t)$ is calculated as

$$T_h'(t,z) = \frac{\mathcal{H}\left(T'(z,t)F(z)\right)}{F(z)}, \tag{3.4}$$

where $\mathcal{H}$ indicates the Hilbert transform operator. $F(z)$ is a weighting function to

suppress the exponential growth of the temperature perturbation, $T'(z,t)$, with altitude and is given by $F(z) = \rho_{(z)}^{1/4}$, where $\rho(z)$ is the atmospheric density obtained from the CIRA86 reference model [*Fleming et al.*, 1990]. Figure 3.3(c) shows $T_h'(z,t)$ and an envelope ($\sqrt{T'^2(z,t) + T_h'^2(z,t)}$). If the observation time is long enough, the number of samples for the ensemble average is sufficiently large, and Eqs. (2.21) and (3.12) yield the same results. However, the statistical error for $E_p$ in Eq. (3.12) is smaller than that in Eq. (2.21), because the number of samples for the ensemble average in Eq. (3.12) is twice as large as that for Eq. (2.21).

Figure 3.3(d) shows an instantaneous $E_p$ profile obtained by the RR lidar at 00 UT on June 27, 2012. Apart from the perturbation due to AGWs, $T'(z,t)$ also includes the error caused by the photon-counting noise (or shot noise). Therefore, a positive bias in $E_p$ could be the result [*Duck et al.*, 2001; *Chu et al.*, 2009; *Yamashita et al.*, 2009]. However, this additional variance of $T'(z,t)$ could be estimated independently. Thus, the corrected $E_p$ values are now estimated in Eq. (3.12).

The observational data with durations longer than 3 h are used for analysis when the hourly temperature error is smaller than 6 K at an altitude of 65 km. Height regions with

temperature errors larger than 1 K are excluded from the $E_p(z)$ analysis to avoid the overestimation of $E_p$(z) at these altitudes for the temperatures derived from the Raman channel. Table 1 shows the total observation time and the number of nights in each month used for this thesis.

# Chapter 4

## 4. AGW Activity at 15 to 70 km Altitude over Syowa (69° S, 40° E), the Antarctic.

This chapter introduces the RR lidar observation results based on *Kogure et al.* [2017]. $E_p$ has been examined at the altitudes of 15–70 km from temperature profiles obtained by the RR lidar at Syowa Station (69° S, 40° E) from May 2011 to October 2013, excluding the austral summer months, using the method introduced in Chapter 3. Here, we will focus on the typical seasonal and vertical variation of the $E_p$ over Syowa.

First, we show the RR lidar observation results, i.e., the temperature and $E_p$ profiles. The $E_p$ above 30 km over Syowa are then compared with those observed by other lidar instruments and the Solar Occultation For Ice Experiment on Aeronomy of Ice in the Mesosphere satellite (SOFIE/AIM). Next, $E_p$ below 30 km is discussed, particularly in terms of its vertical variation. Finally, the remarkable feature of the $E_p$ profile in October 2012 is shown, and the relationship between the seasonal variations of the $E_p$ and the background zonal wind is discussed.

## 4.1 Rayleigh/Raman Lidar Observation Results in 2011–2013

### 4.1.1 Monthly Mean Temperature

Figure 4.1 shows the monthly mean temperature observed by the RR lidar over Syowa from 2011 to 2013. The mean temperature showed similar seasonal and vertical variations each year. The stratopause, where the temperature reached its maximum value, was the highest (~55 km in altitude) and the coldest (250–260 K) around April for two years (2012 and 2013). The stratopause height descended from April to October with increasing temperature. A cold region with a temperature of approximately 190 K or less was observed at around 20 km from June through August, which suggests the possibility of PSC formation above Syowa. The observed temperature structures are similar to those over the southern polar region [*Hitchman et al.*, 1989; *France et al.*, 2012] and Davis station (69° S, 78° E) [*Alexander et al.*, 2011].

### 4.1.2 Monthly Mean $E_p$

Profiles of the monthly mean $E_p$ values between 2011 and 2013 are shown in Figure 4.2. The $E_p$ profile in June of 2011 was excluded, because the statistical fluctuation was too large owing to the limited observation day (see Table 1).

Almost all $E_p$ profiles in Figure 4.2 had a roughly constant exponential slope above the altitude of 30 km. The mean scale height between 35 and 64 km was 11.3 km, averaged over three years, with a standard deviation of 2.6 km. The dotted line in Figure 4.2 indicates a scale height of 11.3 km. The dashed line in Figure 4.2 indicates the slope of the density scale height, $H$ = 7.3 km, which was calculated from the mean temperature between 30 and 70 km over 3 years. This value is smaller than the scale height of $E_p$.

Another distinct feature of the $E_p$ profiles in Figure 4.2 is that most had local maxima at altitudes of approximately 20 km and local minima at altitudes near 25 km. On the other hand, the $E_p$ profile in October 2012 (the right-most line in Figure 4.2(b)) had a local minimum around 40 km, which is much higher than those of the other months.

Figure 4.3 shows the time–altitude sections of the monthly mean $E_p$ from 2011 to 2013. Figure 4.4 shows the day-to-day variations of $E_p$ at 20, 40, and 60 km. The $E_p$ values were logarithmically averaged over the height range of 5.4 km, centered at the target height. $E_p$ above 30 km altitude was maximized in winter (June, July, and August). $E_p$ below 30 km was also maximized in winter (July and August). However, in 2012, the $E_p$ below 30 km exhibited another maximum in October. The interannual variations were smaller than

the seasonal variations, and the day-to-day variations are within a factor of 3 to 4.

### 4.2 Characteristics of AGW over Syowa

#### 4.2.1 Comparison of $E_p$ above 30 km over Antarctica

Here, we compare our results with other lidar and satellite observations over other locations in the Antarctic. These include Rayleigh lidar observations over Davis (69° S, 78° E) [*Alexander et al.*, 2011; *Kaifler et al.*, 2015], Rothera (67° S, 68° W) [*Yamashita et al.*, 2009] and McMurdo (78° S, 167° E) [*Lu et al.*, 2015], and SOFIE/AIM observations between ~63 and 78° S latitude [*Liu et al.*, 2014]. It should be noted that vertical wavelengths and ground-based periods of the extracted GWs were slightly different among these studies. Our study extracted GWs with a $\lambda_z$ of 1.8–16 km and a $\tau$ longer than 2 h. *Alexander et al.* [2011] and *Kaifler et al.* [2015] extracted GWs with $\lambda_z$ = 4–20 km and $\tau$ longer than 2 h. *Yamashita et al.* [2009] did so with a $\lambda_z$ of 2–15 km and a $\tau$ of 1–3 h, and *Lu et al.* [2015] did so with $\lambda_z$ = 2–15 km (i.e., same as *Yamashita et al.* [2009]) and $\tau$ = 2–15 h. Although *Liu et al.* [2014] obtained GWs with a $\lambda_z$ of 2–15 km (i.e., similar to the lidar observations), their horizontal wavelengths were longer than 580 km. This is because the horizontal path length of SOFIE/AIM is

approximately 290 km [*Stevens et al.*, 2012]. The seasonal variation of $E_p$ above 30 km over Syowa showed a maximum value in winter. The timing of maximum $E_p$ is consistent with those acquired at Davis and Rothera, as well as the result of the SOFIE/AIM observations.

The $E_p$ profiles over Syowa in 2011 (purple), 2012 (green), and 2013 (yellow) averaged from May through August are shown in Figure 4.5. The $E_p$ profile over Davis in 2011 is represented by the blue line [*Kaifler et al.*, 2015]. The average profile over Davis in 2007 and 2008 is also indicated in black, as a reference [*Alexander et al.*, 2011]. The scale height of $E_p$ over Syowa between 35 and 64 km in 2011 and 2012 are 9.7 km and 13.7 km, respectively. The scale height in 2013 (13.3 km) is similar to that in 2012. The two profiles acquired over Davis are almost identical and, therefore, the result in 2011 is a typical profile. The scale height of $E_p$ was ~6.8 km between the altitudes of 30 and 40 km, and close to the density scale height. Thus, the scale height of $E_p$ is larger over Syowa than over Davis. The $E_p$ profile taken by SOFIE/AIM (red) for 2007–2013 shows a scale height of 13 km [*Liu et al.*, 2014]. The scale height over McMurdo in 2011 and the average of 2011–2013 are 12.2 and 13 km, respectively (not shown here) [*Lu et al.*, 2015].

These results indicate that the scale height of $E_p$ over Syowa is close to those acquired over McMurdo and by SOFIE/AIM observations, while the scale height taken over Davis is much smaller. This is an interesting result because Syowa and Davis are at almost the same latitude and only 1500 km apart.

It should be noted that the observed $E_p$ values are somewhat different among our study and previous studies (e.g., the value of $E_p$ at 40 km in 2011 was 22 J kg$^{-1}$ over Syowa, but was 12 J kg$^{-1}$ over Davis [*Kaifler et al.*, 2015]). This is probably due to the different vertical resolutions and preprocessing. The height resolution used in *Kaifler et al.* [2015] was 2 km, which was coarser than ours (0.9 km). If a vertical resolution of 2 km is applied, the $E_p$ value over Syowa would be 18 J kg$^{-1}$. In addition, *Kaifler et al.* [2015] applied a high-pass filter with a cutoff wavelength of 20 km to the temperature perturbation profiles, which was not used in our analysis. The $E_p$ value over Davis would be 15 J kg$^{-1}$ without the high-pass filter. The actual difference would be 20% and should not be significant.

### 4.2.2 Seasonal and Vertical Variations of $E_p$ below 30 km

In Section 4.2.1, the $E_p$ value over Syowa indicated local minimum and maximum $E_p$ at approximately 20 and 25 km, respectively. However, the previously reported $E_p$ profile

over Syowa, acquired using radiosondes, did not show a similar local maximum below 25 km [*Yoshiki and Sato*, 2000; *Yoshiki et al.*, 2004]. The height range of our observation was 10–80 km, while the radiosonde observation was between 0 and 30 km. It should also be noted that our analysis used an hourly averaged temperature, while the radiosonde used instantaneous temperature without time averaging. The height average for our lidar was over 0.9 km, but *Yoshiki and Sato* [2000] used standard isobaric and significant levels (the height intervals are 1–2 km). Such a difference could cause different spectral bands to be extracted (in both the time and altitude domains) together with different analysis procedures [*Alexander*, 1998; *Wright et al.*, 2015].

Our results showed that the $E_p$ values of AGWs with a longer period (> 2 h) and a large vertical wavelength (> 1.8 km) had a local maximum of approximately 20 km. *Shibuya et al.* [2015] reported that an inertia-AGW was generated through the spontaneous adjustment to the west of Syowa and propagated through the lower stratosphere over Syowa. Such AGWs possibly contribute to the local maximum of $E_p$ over Syowa.

### 4.2.3 Characteristic $E_p$ Profile in October 2012

As mentioned in the section 4.1.2. the monthly mean $E_p$ profile in October 2012, obtained

by the RR lidar, was different from those of the other months. Figure 4.6a shows the monthly mean $E_p$ profiles acquired using the RR lidar in October from 2011 to 2013. The $E_p$ profile in 2012 is smaller than that in 2011 and 2013 above 35 km. On the other hand, the $E_p$ profile in 2012 has a clear maximum around 25 km, unlike in 2011 and 2013. Such $E_p$ characteristics in 2012 were not due to an outstanding AGW event on a single day, but were seen for four observation days, i.e., 6, 10, 14 and 16 October. To examine the relationship between the $E_p$ profiles and zonal wind distributions, nightly-mean zonal wind profiles on the nights of lidar observations, together with the monthly medians in October from 2011 to 2013, were obtained from MERRA [*Rienecker et al.*, 2011] and are shown in Figures 4.6b–d. The zonal wind at altitudes of 40–50 km in October was close to 0 m $s^{-1}$ on many nights in 2012. However, it was larger than 30 m $s^{-1}$ on most nights in 2011 and 2013. The comparison between the $E_p$ and the zonal wind suggests that GWs with a small ground-based eastward phase speed (i.e., < ~20 m $s^{-1}$) reached their critical level at altitudes of approximately 40–50 km and were prohibited from propagating upward in October 2012. Such a wave could converge below the critical level and obtain a large amplitude and $E_p$ value.

Figure 4.7 shows zonal wind velocities, with a smoothing window of 7 days, over Syowa from September to November in 2011–2013. In 2012, the altitude at which the zonal wind speed was 0 m $s^{-1}$ moved down to 40 km on October 10. Such descents were observed in mid-November 2011 and in late October 2013. Thus, the timing of the descent of the 0-m $s^{-1}$ wind line controls the vertical and seasonal variations in $E_p$ in early spring. These results also suggest that the AGWs with a small ground-based zonal phase speed occupy a large part of the $E_p$ obtained by the RR lidar. We would like to note that *Kaifler et al.* [2015] also observed a decrease in $E_p$ above the altitude of the weak zonal wind over Davis, Antarctica in November 2011.

### 4.3 Conclusion

In this chapter, AGWs with a period longer than 2 h and a vertical wavelength of 1.8–16 km were extracted from temperature profiles obtained by the RR lidar over Syowa Station (69° S, 40° E) between May 2011 and October 2013 in the non-summer months. $E_p$ was estimated for a wide range of altitudes, 15–70 km, to reveal seasonal and vertical variations in AGW activity.

Four features of $E_p$ were revealed: (1) The AGW activity was greater in winter than in

spring and fall, although in 2012, below an altitude of 30 km, the activity was greater in spring than in winter and fall. The seasonal variation in $E_p$ above 30 km is in good agreement with previous studies using Rayleigh lidar at other Antarctic stations. (2) The $E_p$ values above 30 km increased with a mean scale height of 11.3 km. This scale height over Syowa during winter was compared with those over Davis, McMurdo, and the SOFIE/AIM observations over ~63 and 78° S latitude. However, the scale height over Davis (~6.8 km) was much smaller than that of Syowa and close to the density scale height, although Syowa and Davis are located relatively close to each other (~1500 km apart). (3) The $E_p$ profiles at Syowa had local maxima at altitudes near 20 km and local minima at approximately 25 km in almost all months. This feature was persistent but not yet reported by the previous radiosonde studies [*Yoshiki and Sato*, 2000]. Although it is not clear how the local maxima of $E_p$ around 20 km are created, AGW packets generated by spontaneous adjustment to the west of Syowa [*Shibuya et al.*, 2015] could contribute to the local maxima. (4) $E_p$ in October 2012 was smaller at altitudes of 35–60 km and larger at altitudes of 20–35 km than those in 2011 and 2013. We found that the earlier descent of a weak zonal wind layer caused the critical level in October 2012, which is

different than how this particular structure was created in other years.

The RR lidar enabled us to analyze AGWs in a wide height range using the same observation and analysis method. We revealed many features of $E_p$ from the lower stratosphere to the mesosphere over Syowa station, which will contribute to the understanding of AGW vertical propagation, the coupling between lower and upper atmospheres, and the relationship between AGWs and background winds in early spring. This knowledge will help to improve the parameterization scheme. Moreover, we revealed that the scale heights of the $E_p$ of AGWs between Syowa and Davis are quite different, although the two stations are located in close proximity to each other. The reason for this difference will be studied with more observation data acquired using different measurement techniques in the future.

# Chapter 5

## 5. Effects of Horizontal Wind Structure on an AGW Event in the Middle Atmosphere over Syowa (69° S, 40° E), the Antarctic

This chapter focuses on an $E_p$ enhancement event and discusses the day-to-day variation of $E_p$. The nightly mean $E_p$ over Syowa Station (69° S, 40° E) is calculated from temperature profiles observed by the RR lidar over five years (2011–2015) using the method introduced in Chapter 3. We show the enhancement of the $E_p$ values in the upper stratosphere and lower mesosphere on August 8–21, 2014, except August 12. We investigate and discuss the source activity and ray paths of AGW using MERRA, with the aim of revealing the cause of the enhancement. Next, we discuss the depression of the $E_p$ on August 12. This chapter highlights the convergence condition for AGWs, i.e., larger-scale horizontal zonal wind structure and the depression condition for AGW activity, i.e., wind filtering. Finally, we point out a defect in the AGW drag parameterization. These results have been published in Kogure et al. [2018].

### 5.1 Enhancement of $E_p$ in August 2014

Figures 5.1(a), (b), and (c) show the nightly mean $E_p$ at 40, 50, and 60 km, respectively, where the $E_p$ values were logarithmically averaged over an altitude range of 5.4 km, centered at the respective altitudes. The $E_p$ value increased by 2–3 times every 10 km between 40 and 60 km. This increasing rate is equivalent to an $E_p$ scale height of 8–13 km, which is consistent with the results from Chapter 4. The winter (June to August) mean value at each altitude was 2–3 times larger than those during the fall (March to April) and spring (October) periods, as already mentioned in Chapter 4. These results are consistent with previous studies in the Antarctic region [*Kaifler et al.*, 2015; *Kogure et al.*, 2017; *Liu et al.*, 2014; *Zhao et al.*, 2017]. Most of the $E_p$ values for the winter period were within $[Ep]_{winter} \pm \sigma_{winter}$, i.e., 13.3–40.0 J kg$^{-1}$ at 40 km, 23.4–61.4 J kg$^{-1}$ at 50 km, and 65.2–186.9 J kg$^{-1}$ at 60 km, where $[Ep]_{winter}$ is the logarithmic mean of the nightly mean potential energy ($E_p$) in June–August for the five years, and $\sigma_{winter}$ is the logarithmic standard deviation of $E_p$. However, most of the $E_p$ values for August 8–21 in 2014 at 50 and 60 km were larger than $E_p + \sigma_{winter}$.

To investigate this enhancement in more detail, the $E_p$ plots for August 2014 are enlarged as shown in Figures 5.1(d), (e), and (f). The $E_p$ values at 40 km during that month

are comparable to the other years. However, the $E_p$ values at 50 and 60 km for August 8–21, 2014 (except August 12) were larger than the winter mean by more than one standard deviation, i.e., larger than 61.4 J kg$^{-1}$ at 50 km and 186.9 J kg$^{-1}$ at 60 km. The mean value in this period at 60 km (506 J kg$^{-1}$) was about five times as large as the mean value for August 2015 (88 J kg$^{-1}$). Thus, in the next section, we highlight and discuss the causes of this enhancement during August 8–21, 2014 in addition to the depression on August 12.

## 5.2 Influence of Convergence of the AGWs and Critical-Level Filtering

### 5.2.1 Convergence of the AGWs due to the Poleward Tilting of the PNJ with Altitude

One possible cause of the aforementioned enhancement is the existence of an additional GW source for August 8–21, 2014 between 40 and 50 km. A possible source is the spontaneous adjustment near the PNJ region, as it is difficult for other sources, e.g., shear instability, to excite AGWs with longer horizontal wavelength [*Plougonven and Zhang*, 2014].

*Sato and Yoshiki* [2008] and *Murphy et al.* [2014] suggested that large amplitude GWs observed in the lower stratosphere could be emitted by spontaneous adjustment near the imbalance of the PNJ. To investigate this possibility, the residual of the nonlinear balance equation ($|\Delta NBE|$), which indicates the degree of imbalance, was calculated at 1 hPa

(~43 km altitude) and 0.5 hPa (~47 km altitude) above Syowa. This is the same approach as *Zhang* [2004] from MERRA. The calculation of $|\Delta NBE|$ is described in more detail in Appendix A. Figure 5.2 shows $|\Delta NBE|$ at 1 hPa (~43 km altitude) and 0.5 hPa (~47 km altitude) above Syowa in August 2014. The $|\Delta NBE|$ values during the AGW enhancement were $4.7 \times 10^{-9}$ $s^{-2}$ and $6.0 \times 10^{-9}$ $s^{-2}$ on average at 1 hPa and 0.5 hPa, respectively. They are smaller than the values for August 1–7, 2014 before the enhancement ($9.0 \times 10^{-9}$ $s^{-2}$ at 1 hPa and $1.0 \times 10^{-8}$ $s^{-2}$ at 0.5 hPa on average, respectively). Another possibility is that the observed AGW enhancement over Syowa was caused by the convergence of AGW packets propagating from lower and higher latitudes as a result of their meridional propagation. Since the AGWs observed by the RR lidar have a long wave period, i.e., longer than 2 h, they can travel a long horizontal distance during their upward propagation. We evaluated this possibility by analyzing the ray paths of the AGWs based on the ray-tracing method of *Dunkerton* [1984] and compared the results in the enhancement period (August 8–21, 2014) with those in August 2015. The nightly mean wind and temperature fields acquired from MERRA for each observation date on August 8–21, 2014 and August 2015 were used as the background

for the ray-tracing procedure. It was also assumed that the background fields were uniform in longitude. The AGWs were emitted upward from 10 km between 20° S and 80° S at 5° intervals. The initial horizontal wavelength and ground-based period were assumed to be 1000 km and 10 h, respectively, because such large-scale GWs are typically detected by lidar [*Gardner et al.*, 1998; *Wilson et al.*, 1991]. An initial *k* value, i.e., zonal wavenumber, was assumed to be negative, i.e., westward. The AGWs with a more westward wavenumber in the lower latitudes than in the PNJ are refracted to the higher latitudes as a result of the meridional gradient of zonal wind. On the other hand, the AGWs in the higher latitudes are refracted to the lower latitudes, i.e., such waves are refracted toward the PNJ [*Dunkerton*, 1984; *Ehard et al.*, 2017; *Sato et al.*, 2009]. Moreover, AGWs with an eastward wavenumber generally encounter their critical level in the middle atmosphere, thus, they are not considered here. The initial *l* value, i.e., meridional wavenumber, was also assumed to be negative, i.e., southward, because the AGW activity in the lower stratosphere, i.e., near the sources, at the lower latitudes (< 69° S) is generally greater than the activity near the south polar regions (> 69° S) [*Alexander et al.*, 2016; *Allen and Vincent*, 1995; *Tsuda et al.*, 2000]. The initial direction

of the horizontal wavenumber vector was, therefore, assumed to be southwestward. The calculation of the ray-tracing method is described in more detail in Appendix B.

Figure 5.3 shows the altitude-latitude sections of the nightly mean zonal wind at the longitude of Syowa (40° E) on (a) August 1–7, 2014 and (b) August 8–21, 2014, and the monthly mean wind in (c) August 2015. White and black lines indicate the parts of the rays where the GWs have a vertical wavelength within and outside 1.8–16 km, respectively. In Figure 5.3(b), most of the GWs converged over Syowa at approximately 55 km. However, some of the GWs converged over 65° S, shown in Figure 5.3(a), and such a convergence did not appear in the case shown in Figure 5.3(c). This could be accounted for if the PNJ in Figure 5.3(b) tilts poleward with altitude from ~50° S to ~70° S, and the AGWs with westward wavenumbers are refracted toward ~70° S. The PNJ shown in Figure 5.3(b) tilts more than that shown in Figure 5.3(a), which suggests that the AGWs in August 1–7, 2014, have a greater preference to propagate into the higher latitudes than those in August 7–21, 2014. It should be noted that the PNJ region shown in Figure 5.3(c) tilts equatorward with altitude from ~40° S to ~60° S. Under such a condition, the AGWs are refracted toward ~40° S. We also checked the case for 2011,

2012, and 2013, but no convergence was found (not shown). This is probably because the PNJ did not tilt poleward with altitude. There is a possibility that the AGWs with other initial wave parameters contributed to the enhancement of $E_p$ values, because some studies (e.g., *Nicolls et al.* [2010] and *Chen et al.* [2013]) report that AGWs with equatorward wavenumbers propagated from the pole to mid-latitude. The ray paths of the AGW with other initial wavenumber, ground-based period, and azimuth angle were also analyzed during the enhancement and August 2015 (not shown). The results during the enhancement show the convergence of the AGWs with 1000–2500 km horizontal wavelengths, 10–20 h ground-based periods, and 205–23 ° azimuth angles (i.e., clockwise from North). The AGW parameters were similarly varied for the case of August 2015. However, the AGWs did not converge. Thus, we conclude that the enhanced AGWs shown in Figure 5.1 are due to the convergence of AGW packets with southwestward wavenumbers.

### 5.2.2 Critical-Level Filtering by a Synoptic Scale Disturbance on August 12, 2014

The $E_p$ value on August 12, 2014 was much smaller than the value of the other days during August 8–21 despite a tilted PNJ, similar to the condition of Figure 5.3(a). It is notable that the behavior of the meridional wind at Syowa on August 12 was unusual.

Figure 5.4 shows a time-altitude section of the meridional wind over Syowa during the enhancement. The meridional wind at approximately 50 km was primarily confined to −40 and 0 m $s^{-1}$ on the lidar observation days. However, on August 12 the meridional wind changed drastically from +56 m $s^{-1}$ to −70 m $s^{-1}$. Horizontal maps of these winds at 0.5 hPa near this meridional wind change are shown in Figure 5.5(a), in which the meridional wind disturbance at a horizontal scale of ~4000 km is clearly seen near Syowa, moving eastward. The passage of this disturbance drastically changed the meridional wind from −80 m $s^{-1}$ to +80 m $s^{-1}$ in the region between 55 and 75° S, throughout which the AGWs with a non-zero meridional wavenumber could easily reach their critical level. Thus, it is concluded that the depression of the AGW activity on August 12 was likely due to the passage of a synoptic-scale disturbance in the upper stratosphere over Syowa.

**5.3. Conclusion**

The nightly mean $E_p$ over Syowa Station (69° S, 40° E) was calculated from the temperature profiles observed by the RR lidar over a five-year period from 2011 to 2015, except the summer periods. It was observed that $E_p$ for August 8–21, 2014, except August 12, was significantly larger than the winter mean. The results of ray-tracing analysis revealed the possibility of convergence of longer-horizontal-wavelength AGWs,

with the southwestward wavenumbers near ~55 km altitude over Syowa, emitted from various latitudes. This suggests that the AGWs were refracted toward Syowa by the poleward tilting of the PNJ region with altitude. It was also observed that the $E_p$ value obtained on August 12 was the smallest recorded value during the enhancement. This depression of AGW activity could be caused by a synoptic disturbance passing over Syowa.

It was demonstrated that AGW activity in the Antarctic upper stratosphere and lower mesosphere can be significantly enhanced by the meridional propagation of AGWs, i.e., refraction, and suppressed by local wind fields due to a synoptic-scale disturbance, i.e., critical-level filtering. Although horizontal propagation has not been taken into account for GCMs, it has the potential to cause day-to-day variations in AGW activity; in other words, it has the potential to cause intermittency of the AGWs.

## 6. Summary and Conclusions

The purpose of this thesis is to reveal the physical characteristics of the AGW over Syowa (69° S, 40° E), in the Antarctic, from RR lidar observation. This thesis focused on the relationship between the AGW and the background wind condition.

In Chapter 1, the atmospheric wind and temperature structure in the middle atmosphere, which are created by the Rossby wave and the AGW, are introduced. The Rossby wave and baroclinic wave drive the stratospheric circulation (Brewer-Dobson circulation). The AGW drives not only the summer to winter pole circulation in the mesopause region but also affects the Brewer-Dobson circulation. Interaction between these waves and the background atmospheric field is crucial to reproduce the realistic middle atmosphere in the models. The Rossby wave can be explicitly resolved by the practical numerical models. On the other hand, some of the AGWs cannot be explicitly resolved in the GCMs due to coarseness of the grids, so that their effect is parameterized in the practical models. However, the parameterizations are inaccurate, degrading the reliability of a prediction of a climate trend, and should be constrained based on the observations.

In Chapter 2, the characteristics of AGWs (e.g., critical and turning levels) are introduced

based on linear theory. The critical and turning levels influence the vertical propagation of AGWs. Then, we introduced the previous lidar and satellite studies. The satellite studies have shown that the region around ~60° S is one of the hot spots of AGWs during winter. However, the causes are not well understood, which could lead to the parameterization scheme inaccurately representing the AGW effect. Its two possible causes are introduced: the inaccurate representation of the AGW source and the neglect of the horizontal propagation. To examine the propagation, sources, and characteristics of AGW over the higher latitudes in the southern hemisphere, this thesis focuses on two aspects—the relationship between the AGWs and the background wind, and the causes of intermittency.

In Chapter 3, the specification of the RR lidar system, methodology to derive temperature profiles from the RR lidar data, and analysis method of AGW activity were introduced. The RR lidar can observe the temperature between the altitudes of 10 and 80 km. Temperature perturbations of AGW were derived from the observed temperature profile to calculate the $E_p$, which indicates the activity of the AGW. We also applied the Hilbert transform weighted by the atmospheric density to the calculation of $E_p$ to reduce its

statistical error.

In Chapter 4, the $E_p$ values between May 2011 and October 2013, except those during the summer months, were calculated and investigated. These results revealed four features: (1) The AGW activity was larger in winter than in spring and fall, except at altitudes below 30 km in 2012. (2) The $E_p$ values above 30 km increased with a mean scale height of 11.3 km. This scale height is larger than that at the Davis station, although these stations are located relatively close to each other (~1500 km). (3) The $E_p$ profiles had local maxima near an altitude of 20 km and local minima around 25 km. (4) The $E_p$ values in October 2012 are smaller in the altitude range of 35–60 km and larger in the range of 20–35 km than those in 2011 and 2013. This vertical feature could be caused by the critical level at ~35 km, at which the zonal wind is weak.

In Chapter 5, the $E_p$ values were calculated and analyzed over five years (2011–2015). It was found that the $E_p$ values between 50 and 60 km for August 8–21, 2014, except on August 12, were larger than those during the winter mean by one order of magnitude. A ray-tracing analysis indicated the possibility that the AGWs with long horizontal wavelength converged near ~55 km altitude over Syowa, which suggests that the AGWs

were refracted toward Syowa by the poleward tilt of the PNJ with altitude. The PNJ condition on August 12 was similar to that during the enhancement, but the depression of the $E_p$ could be caused by critical-level filtering due to the synoptic-scale disturbance.

The RR lidar enabled us to analyze the AGWs in a wide height range and reveal the many features of the AGW activity over the Antarctic. We also revealed the relationship between the AGW activity and the wind fields with re-analysis data, i.e., MERRA. These results will help us to constrain the AGW parameters (e.g., their amplitude and propagation direction). In addition, this thesis suggests that the horizontal propagation is one of causes of AGW intermittency.

To extend this study, we propose four open questions to be examined in our future work.

(1) What creates the local maxima of $E_p$ near the 20-km altitude?

It was shown that the $E_p$ profiles over Syowa exhibited local maxima at an altitude of approximately 20 km. This feature was not reported by previous radiosonde studies, although it was persistent. This feature could indicate that the AGW contributes to the lower stratospheric circulation, and the contribution is probably greater than believed. Moreover, the source activity could be higher in the upper troposphere and the lower

stratosphere than suggested because the dissipation of the AGW at ~25 km altitude has been overlooked. To reveal the cause, we need to understand the propagation directions and sources of the AGW in the lower stratosphere. We believe that Doppler lidar, radiosondes, and PANSY radar will help us to reveal that. Those instruments will enable us to investigate the wave parameters (e.g., the horizontal wavelength and the frequency). Those parameters will provide knowledge of the propagation characteristics of the AGW near the 20-km altitude over Syowa. In addition, the parameters will enable us to investigate the source of those waves by using the ray-tracing method. This future study will help us to understand the factors, which cause the vertical variation in AGW activity in the upper troposphere and the lower stratosphere.

(2) What causes the longitude variation in AGW activity?

This thesis showed that the scale height of $E_p$ at Syowa was twice that at Davis, although both stations are located relatively close to each other (~1500 km). *Matsuda et al*. [2017] also reported that the phase speed spectra in the mesopause obtained by OH airglow imagers vary between the two stations; but their analysis period was very short (i.e., 1.5 months). This longitude variation might be caused by longitudinally dependent wave

sources and propagation conditions. To reveal how the AGWs at the two stations differ and why, we compare data from radar, imagers, and lidar. Then, we investigate the differences in the propagation process and source activity of AGW using re-analysis data and high-resolution models. As a first step, we have already compared data from the OH imagers at Syowa and Davis, and we are investigating the sources and passes of AGW using a new re-analysis tool, i.e., the Modern-Era Retrospective analysis for Research and Applications, Version 2 (MERRA-2) reanalysis product.

(3) Proposal of lidar observations below the core of PNJ (that is, ~60° S)

This thesis found one enhancement event of AGW activity during the five years of study. We believe that the AGW more frequently converges at 55–65° S, at latitudes 5–15° lower than that of Syowa, because the PNJ structure is generally similar to those shown in Figure 5.3(c). We would like to propose installing Rayleigh lidar on an island in the Antarctic ocean (e.g., Bouvet Island). We believe that the lidar on those islands will be able to more frequently observe the enhancement of AGW activity and AGWs propagating from the lower latitudes. This study will reveal the interaction between the wave sources in the low and middle latitudes and the AGW activity in the high latitudes.

(4) How does the source activity influence the AGW activity and its characteristics?

This thesis focused on the propagation conditions and suggested that they strongly influence the AGW activity, causing day-to-day variation. In addition, their source activity also causes spatial and temporal variation in the AGW activity. Their sources can be separated into two types, namely, orographic and non-orographic sources. The relationship among topography, wind, and orographic AGWs are theoretically understood [*Nappo*, 2013], but the relationship between atmospheric phenomena and non-orographic AGWs is not understood well. The atmospheric condition needs to be linked with the parameters of the non-orographic AGW. However, there are two challenges: (i) It is difficult to determine the sources of the AGW, especially in the middle, because some of the AGWs observed in the middle atmosphere could propagate a long distance. (ii) The observations do not follow the propagation of a specific AGW packet, from its source region to the middle atmosphere. We would like to propose the “one life cycle of AGW” research plan. The plan tries to follow a specific AGW packet by using several kinds of observations (i.e., ground-based and satellite remote sensing, and balloon observations) and the ray-tracing method with reanalysis data. For example, the specific AGW packet

is observed by radiosonde in the lower stratosphere, i.e., probably near its source. Then, its source is determined through reanalysis, and the wave parameters are derived. Its forward path can be calculated by the ray-tracing method. Finally, the wave parameters estimated by the method are compared with the observations if the observation points are on that path. Such a study would highlight not only the relationship between the source activity and the AGW activity in the middle atmosphere but also the variation in AGW parameters (e.g., its amplitude and horizontal wavenumbers) in the propagation.

**Appendix A. Residual of the Nonlinear Balance Equation (ΔNBE)**

The residual of the nonlinear balance equation (ΔNBE) indicates the degree of imbalance. One of primary generation mechanism for AGWs is that the unbalanced flow emits the AGW to return to a state of balance. Residual ΔNBE, which is applicable on short time scales and includes the effect of flow curvature, is commonly used as an unbalanced flow diagnostic.

The divergence equation in the pressure coordinate is given as:

$$\frac{\mathrm{D}(\nabla \cdot \boldsymbol{v})}{\mathrm{Dt}} = \nabla \cdot (\boldsymbol{f} \times \boldsymbol{v}) - \nabla^2 \Phi \qquad \text{(A.1)}$$

where $\boldsymbol{v}\ (= (u, v, w_p))$ is the wind velocity, $\boldsymbol{f}$(= (0, 0, -$f$ )) is the Coriolis parameter, and $\Phi$ is the geopotential. Variable $w_p (= \frac{\mathrm{d}p}{\mathrm{d}t})$ is the vertical wind in the pressure coordinate. Eq. (A.1) can be rewritten as (*Zhang et al*, 2004; *Moore and Abeling*, 1988)

$$\frac{\partial D}{\partial t} = \qquad \text{(A.2)}$$

$$-(\boldsymbol{v} \cdot \nabla)D - w_p \frac{\partial D}{\partial P} + D^2 - \left(\frac{\partial \boldsymbol{v}}{\partial P} \cdot \nabla\right) w_p + 2J(u, v) - \beta u + f\zeta - \nabla^2 \Phi$$

where $D$ is $\nabla \cdot \boldsymbol{v}$, $J(u, v)$ is the Jacobian, $\beta (= \frac{\partial f}{\partial y})$ is the Rossby parameter, and $\zeta (= \nabla \times \boldsymbol{v_h})$ is the relative vorticity. Eq. (A.2) describes the relationship between the degree of large-scale imbalance and the response of the atmosphere to the imbalance through the

divergence and vertical motion. The first to fourth terms on the right hand correspond to the response of the atmosphere to the imbalance. The fifth to eighth terms correspond to the lack of large-scale imbalance, and the sum of these terms is called $\Delta\mathrm{NBE}$. Thus, $\Delta\mathrm{NBE}$ is defined as

$$\Delta\,\mathrm{NBE} \equiv 2J(u,v) - \beta u + f\zeta - \nabla^2\Phi. \tag{A.3}$$

$\Delta\mathrm{NBE}$ can be computed with the numerical model and reanalysis data using Eq. (A.3).

**Appendix B. Ray-tracing method for the AGWs**

The propagation of the AGW is examined in Chapter 5, with a ray-tracing method introduced by Dunkerton [1984]. This method calculates the ray path of an AGW based on the following equations,

$$\hat{\omega}(\boldsymbol{x}, t) = \omega - \overline{\boldsymbol{u_h}} \cdot \boldsymbol{k_h} \tag{B.1}$$

$$m^2 = \frac{|\boldsymbol{k_h}|^2 (N^2 - \hat{\omega}^2)}{(\hat{\omega}^2 - f^2)} - \frac{1}{4H^2} \tag{B.2}$$

$$\frac{\mathrm{d}k}{\mathrm{d}t} = -\left(k\frac{\partial \bar{u}}{\partial x} + l\frac{\partial \bar{v}}{\partial x}\right) \tag{B.3}$$

$$\frac{\mathrm{d}l}{\mathrm{d}t} = -\left(k\frac{\partial \bar{u}}{\partial y} + l\frac{\partial \bar{v}}{\partial y} + \frac{\beta f}{\hat{\omega}}\right) \tag{B.4}$$

$$\boldsymbol{u_{h_g}} = \frac{(N^2 - \hat{\omega}^2)\boldsymbol{k_h}}{(|\boldsymbol{k_h}|^2 + m^2 + \frac{1}{4H^2})\,\hat{\omega}} + \overline{\boldsymbol{u_h}} \tag{B.5}$$

$$w_g = -\frac{m(\hat{\omega}^2 - f^2)}{(|\boldsymbol{k_h}|^2 + m^2 + \frac{1}{4H^2})\,\hat{\omega}} \tag{B.6}$$

where the parameters in Eqs. (B.1)–(B.6) are shown in Table A1, and $\frac{\mathrm{d}}{\mathrm{d}t}$ indicates the time rate of change of the parameter it is applied to. Eq. (B.2) is called the dispersion relation for AGWs, which describes the relation between the wavenumber and frequency. Horizontal refraction is expressed and calculated by Eqs. (B.3) and (B.4). The initial value of $\omega$ and $\boldsymbol{k_h}$ are substituted in these equations, and these equations can be integrated in time using the Runge-Kutta method. The background fields are calculated as follows:

(1) The background wind and temperature fields are acquired from MERRA.

(2) The zonal and meridional differentials are calculated using symmetric central differencing, and the vertical differentials are computed using asymmetric central differencing.

(3) These values are interpolated at specific **x** and t by bilinear interpolation horizontally and cubic spline interpolation in vertical space and time.

The calculation is terminated when the AGW encounters the turning level ($m^2 \rightarrow 0$; $m^2 \leq 0$ [$m^{-2}$] in our program), the critical level ($m^2 \rightarrow \infty$; $m^2 \geq 3.4 \times 10^{38}$ [$m^{-2}$] in our program), or the second pressure level (i.e., 0.2 hPa) from the top.

Table B.1. Parameters in Eq. (1)–(6)

$\boldsymbol{x} = (x, y, z)$

$x$ : Positive eastward

$y$ : Positive northward

$z$ : Altitude

$t$ : Time

$\overline{\boldsymbol{u_h}} = (\bar{u}, \bar{v})$

$\bar{u}$ : Background zonal wind

$\bar{v}$ : Background meridional wind

$\boldsymbol{u_{hg}} = (u_g, v_g)$

$u_{\mathrm{g}}$ : Ground-based zonal group velocity of AGW

$v_{\mathrm{g}}$ : Ground-based meridional group velocity of AGW

$k$ : Zonal wavenumber of AGW

$l$ : Meridional wavenumber of AGW

$m$ : Vertical wavenumber of AGW

$N$ : Brunt–Väisälä frequency

$H$ : Scale height of the atmospheric density

$f$ : Coriolis frequency

$\beta (= {}^{\partial f}/_{\partial y})$ : Rossby parameter

$\hat{\omega}$ : Intrinsic frequency of AGW

$\omega$ : Ground-based frequency of AGW

**References**

Alexander, M. J. (1998), Interpretations of observed climatological patterns in stratospheric gravity wave variance. *J. Geophys. Res.*, 103(*D8*), *8627–8640*, doi:10.1029/97JD03325.

Alexander, M. J., Eckermann, S., Ern, M., Geller, M., Kawatani, Y., McLandress, C., et al. (2010). Recent developments in gravity wave effects in climate models and the global distribution of gravity wave momentum flux from observations and models. *Q.J.R. Meteorol. Soc.*, 136: 1103–1124, doi:10.1002/qj.637.

Alexander, S. P., A. R. Klekociuk, and T. Tsuda (2009), Gravity wave and orographic wave activity observed around the Antarctic and Arctic stratospheric vortices by the COSMIC GPS-RO satellite constellation. *J. Geophys. Res.*, 114, D17103, doi: 10.1029/2009JD011851.

Alexander, S. P., A. R. Klekociuk, and D. J. Murphy (2011), Rayleigh lidar observations of gravity wave activity in the winter upper stratosphere and lower

mesosphere above Davis, Antarctica (69° S, 78° E). *J. Geophys. Res.*, 116, D13109, doi:10.1029/2010JD015164.

Alexander, S. P., K. Sato, S. Watanabe, Y. Kawatani, and D. J. Murphy (2016), Southern Hemisphere extratropical gravity wave sources and intermittency revealed by a middle-atmosphere general circulation model. *J. Atmos. Sci.*, 73, 1335–1349, doi:10.1175/JAS-D-15-0149.1.

Allen, S. J., and R. A. Vincent (1995), Gravity wave activity in the lower atmosphere: Seasonal and latitudinal variations. *J. Geophys. Res.*, 100(D1), 1327–1350, doi:10.1029/94JD02688.

Andrews, D., J. Holton, and C. Leovy (1987), Middle Atmosphere Dynamics. *Academic Press, Orlando, Fl.*

Ansmann, A., M. Riebesell, and C. Weitkamp (1990), Measurement of atmospheric aerosol extinction profiles with a Raman lidar. *Opt. Lett.* 15: 746–748.

Ansmann, A., M. Riebesell, U. Wandinger, C. Weitkamp, E. Voss, W. Lahmann, and W. Michaelis (1992), Combined Raman elastic-backscatter lidar for vertical profiling

of moisture, aerosol extinction, backscatter, and lidar ratio. *Appl. Phys. B*, *55*(1), 18–28.

Baumgaertner, A. J. G., and A. J. McDonald (2007), A gravity wave climatology for Antarctic compiled from Challenging Minisatellite Payload Global Positioning System (CHAMP/GPS) radio occultations. *J. Geophys. Res.*, 112, D05103, doi:10.1029/2006JD007504.

Baumgarten, G., J. Fiedler, J. Hildebrand, and F.-J. Lübken (2015), Inertia gravity wave in the stratosphere and mesosphere observed by Doppler wind and temperature lidar. *Geophys. Res. Lett.*, 42, 10,929–10,936, doi: 10.1002/2015GL066991.

Bracewell, R. (1999), The Fourier Transform and Its Applications. *McGraw-Hill*, 640 pp.

Bucholtz, A. (1995), Rayleigh-scattering calculations for the terrestrial atmosphere. *Appl. Opt.*, 24, 2773.

Bühler, O., and M. McIntyre (2003), Remote recoil: A new wave–mean interaction effect. *J. Fluid Mech.*, 492, 207–230, doi:10.1017/S0022112003005639.

Butchart, N., A. J. Charlton-Perez, I. Cionni, S. C. Hardiman, P. H. Haynes, K. Krüger, et al. (2011), Multimodel climate and variability of the stratosphere. *J. Geophys. Res.*

*Atmos.*, 116, D05102, doi:10.1029/2010JD014995.

Chanin, M.-L., and A. Hauchecorne (1981), Lidar observation of gravity and tidal waves in the stratosphere and mesosphere. *J. Geophys. Res.*, 86(C10), 9715–9721, doi:10.1029/JC086iC10p09715.

Chen, C., X. Chu, A. J. McDonald, S. L. Vadas, Z. Yu, W. Fong, and X. Lu (2013), Inertia-gravity waves in Antarctica: A case study using simultaneous lidar and radar measurements at McMurdo/Scott Base (77.8° S, 166.7° E). *J. Geophys. Res.*, 118, 2794–2808, doi:10.1002/jgrd.50318.

Chu, X., C. Yamashita, P. J. Espy, G. J. Nott, E. J. Jensen, H.-L. Liu, W. Huang, and J. P. Thayer (2009), Responses of polar mesospheric cloud brightness to stratospheric gravity waves at the South Pole and Rothera, Antarctica. *J. Atmos. Sol. Terr. Phys*., 71, 434–445, doi:10.1016/j.jastp.2008.10.002.

Chu, X., J. Zhao, X. Lu, V. L. Harvey, R. M. Jones, E. Becker, et al. (2018), Lidar observations of stratospheric gravity waves from 2011 to 2015 at McMurdo (77.84° S, 166.69° E), Antarctica: 2. Potential energy densities, lognormal distributions, and seasonal variations. *J. Geophys. Res. Atmos.*, 123, 7910–

7934, https://doi.org/10.1029/2017JD027386.

Duck, T. J., J. A. Whiteway, and A. I. Carswell (2001), The gravity wave-Arctic stratospheric vortex interaction. *J. Atmos. Sci.*, 58, 3581–3596, doi:10.1175/1520-0469(2001)058<3581:TGWASV>2.0.CO;2.

Dunkerton, T. (1978), On the mean meridional mass motions of the stratosphere and mesosphere. *J. Atmos. Sci.*, 35, 2325–2333, https://doi.org/10.1175/1520-0469(1978)035<2325:OTMMMM>2.0.CO;2.

Dunkerton, T. J. (1984), Inertia–gravity waves in the stratosphere. *J. Atmos. Sci.*, 41, 3396–3404, doi:10.1175/1520 0469(1984)041<3396:IWITS>2.0.CO;2.

Ehard, B., B. Kaifler, N. Kaifler, and M. Rapp (2015), Evaluation of methods for gravity wave extraction from middle-atmospheric lidar temperature measurements. *Atmos. Meas. Tech.*, 8, 4645–4655, doi:10.5194/amt-8-4645-2015.

Ehard, B., B. Kaifler, D. Andreas, P. Preusse, N. Kaifler, S. D. Eckermann, M. Bramberger, et al. (2017), Horizontal propagation of large-amplitude mountain waves into the polar night jet. *J. Geophys. Res. Atmos.*, 122, 1423–1436, doi:10.1002/2016JD025621.

Ern, M., P. Preusse, J. C. Gille, C. L. Hepplewhite, M. G. Mlynczak, J. M. Russell III,

and M. Riese (2011), Implications for atmospheric dynamics derived from global observations of gravity wave momentum flux in stratosphere and mesosphere. *J. Geophys. Res.*, 116, D19107, doi: 10.1029/2011JD015821.

Fleming, E. L., S. Chandra, J. J. Barnett, and M. Corney (1990), COSPAR international reference atmosphere. Chap. 2, Zonal mean temperature, pressure, zonal wind, and geopotential height as a function of latitude, *Adv. Space Res*., 10(12), 11–59.

France, J. A., V. L. Harvey, C. E. Randall, M. H. Hitchman, and M. J. Schwartz (2012), A climatology of stratopause temperature and height in the polar vortex and anticyclones. *J. Geophys. Res.*, 117, D06116, doi:10.1029/ 2011JD016893.

Fritts, D. C., and M. J. Alexander (2003), Gravity wave dynamics and effects in the middle atmosphere, *Rev. Geophys.*, 41, 1003, doi:10.1029/2001RG000106.

Garcia, R. R., A. K. Smith, D. E. Kinnison, D. J. Murphy, and Á. de la Cámara (2017), Modification of the gravity wave parameterization in the whole atmosphere community climate model: Motivation and results, *J. Atmos. Sci.*, 74(1), 275–291, doi:10.1175/JAS-D-16-0104.1.

Gardner, C. S., and M. J. Taylor (1998), Observational limits for lidar, radar, and airglow imager measurements of gravity wave parameters, *J. Geophys. Res.*, 103(D6), 6427–6437, doi:10.1029/97JD03378.

Gardner, C. S., M. S. Miller, and C. H. Liu (1989), Rayleigh lidar observations of gravity wave activity in the upper stratosphere at Urbana, Illinois. *J. Atmos. Sci.*, 46, 1838–1854, https://doi.org/10.1175/1520-0469(1989)046<1838:RLOOGW>2.0.CO;2.

Geller, M. A., M. J. Alexander, P. T. Love, J. Bacmeister, M. Ern, A. Hertzog, E. Manzini, P. Preusse, K. Sato, A. A. Scaife, and T. Zhou (2013), A comparison between gravity wave momentum fluxes in observations and climate models, *J. Clim.*, 26, 6383–6405, doi:10.1175/JCLI-D-12-00545.1.

Hauchecorne, A., and M. L. Chanin (1980), Density and temperature profiles obtained by lidar between 35 and 70 km, *Geophys. Res. Lett.*, 7(8), 565–568, doi:10.1029/GL007i008p00565.

Hendricks, E. A., J. D. Doyle, S. D. Eckermann, Q. Jiang, and P. A. Reinecke (2014), What Is the source of the stratospheric gravity wave belt in austral winter? *J. Atmos. Sci.*, 71, 1583–1592, https://doi.org/10.1175/JAS-D-13-0332.1.

Hertzog, A., R. Plougonven, and M. J. Alexander (2012), On the intermittency of gravity wave momentum flux in the stratosphere. *J. Atmos. Sci.*, 69, 3433–3448, doi:10.1175/JAS-D-12-09.1.

Hitchman, M. H., J. C. Gille, C. D. Rodgers, and G. Brasseur (1989), The separated polar winter stratopause: A gravity wave driven climatological feature, *J. Atmos. Sci.*, 46, 410–422.

Hoffmann, L., X. Xue, and M. J. Alexander (2013), A global view of stratospheric gravity wave hotspots located with Atmospheric Infrared Sounder observations, *J. Geophys. Res. Atmos.*, 118, 416–434, doi: 10.1029/2012JD018658.

Holton, J. R. (1983), The influence of gravity wave breaking on the general circulation of the middle atmosphere, *J. Atmos. Sci*., 40(10), 2497–2507, doi:10.1175/1520-0469(1983)040<2497:TIOGWB>2.0.CO;2.

Holton, J. R. (1992), An Introduction to Dynamic Meteorology. *Academic Press*, San Diego, New York.

Holton, J. R., P. H. Haynes, M. E. McIntyre, A. R. Douglass, R. B. Rood, and L. Pfister (1995), Stratosphere‐troposphere exchange, *Rev. Geophys.*, 33(4), 403–439, doi: 10.1029/95RG02097.

Kaifler, B., F. J. Lübken, J. Höffner, R. J. Morris, and T. P. Viehl (2015), Lidar observations of gravity wave activity in the middle atmosphere over Davis (69° S, 78° E), Antarctica, *J. Geophys. Res. Atmos*., 120, 4506–4521, doi:10.1002/2014JD022879.

Kalisch, S., P. Preusse, M. Ern, S. D. Eckermann, and M. Riese (2014), Differences in gravity wave drag between realistic oblique and assumed vertical propagation, *J. Geophys. Res. Atmos.*, 119, 10,081–10,099, *doi:*10.1002/2014JD021779.

Kogure, M., T. Nakamura, M. K. Ejiri, T. Nishiyama, Y. Tomikawa, M. Tsutsumi, H. Suzuki, T. T. Tsuda, T. D. Kawahara, and M. Abo (2017), Rayleigh/Raman lidar observations of gravity wave activity from 15 to 70 km altitude over Syowa (69° S,

40° E), the Antarctic, *J. Geophys. Res. Atmos.*, 122, 7869–7880, doi: 10.1002/2016JD026360.

Kogure, M., T. Nakamura, M. K. Ejiri, T. Nishiyama, Y. Tomikawa, and M. Tsutsumi (2018), Effects of horizontal wind structure on a gravity wave event in the middle atmosphere over Syowa (69° S, 40° E), the Antarctic. *Geophys. Res. Lett.*, 45, 5151–5157. https://doi.org/10.1029/2018GL078264.

Leovy, C. (1964), Simple models of thermally driven mesospheric circulation. *J. Atmos. Sci.* 21(4), 327–341.

Li, T., T. Leblanc, I. S. McDermid, D. L. Wu, X. Dou, and S. Wang (2010), Seasonal and interannual variability of gravity wave activity revealed by long-term lidar observations over Mauna Loa Observatory, Hawaii, *J. Geophys. Res.*, 115, D13103, doi:10.1029/2009JD013586.

Lindzen, R. S. (1981), Turbulence and stress owing to gravity wave and tidal breakdown, *J. Geophys. Res.*, 86(C10), 9707–9714, doi:10.1029/JC086iC10p09707.

Liu, X., J. Yue, J. Xu, L. Wang, W. Yuan, J. M. Russell III, and M. E. Hervig (2014), Gravity wave variations in the polar stratosphere and mesosphere from SOFIE/AIM temperature observations, *J. Geophys. Res. Atmos.*, 119, doi:10.1002/2013JD021439.

Lu, X., X. Chu, W. Fong, C. Chen, Z. Yu, B. R. Roberts, and A. J. McDonald (2015), Vertical evolution of potential energy density and vertical wave number spectrum of Antarctic gravity waves from 35 to 105 km at McMurdo (77.8° S, 166.7° E), *J. Geophys. Res. Atmos.*, 120, 2719–2737.

Matsuda, T. S., T. Nakamura, M. K. Ejiri, M. Tsutsumi, Y. Tomikawa, M. J. Taylor, Y. Zhao, P.-D. Pautet, D. J. Murphy, and T. Moffat-Griffin (2017), Characteristics of mesospheric gravity waves over Antarctica observed by Antarctic Gravity Wave Instrument Network imagers using 3-D spectral analyses, *J. Geophys. Res. Atmos.*, 122, 8969–8981, doi:10.1002/2016JD026217.

Moore, J. T. and W. A. Abeling (1988), A Diagnosis of Unbalanced Flow in Upper Levels during the AYE-SESAME I Period. *Mon. Wea. Rev.*, **116**, 2425–2436, https://doi.org/10.1175/1520-0493(1988)116<2425:ADOUFI>2.0.CO;2.

Murphy, D. J., S. P. Alexander, A. R. Klekociuk, P. T. Love, and R. A. Vincent (2014),

Radiosonde observations of gravity waves in the lower stratosphere over Davis, Antarctica, *J. Geophys. Res. Atmos.*, 119(21), 11,973–11,996, doi:10.1002/2014JD022448.

Nappo, C. J. (2013), An Introduction to Atmospheric Gravity Waves. *Academic Press, Orlando, Fl*.

Nicolls, M. J., R. H. Varney, S. L. Vadas, P. A. Stamus, C. J. Heinselman, R. B. Cosgrove, and M. C. Kelley (2010), Influence of an inertia-gravity wave on mesospheric dynamics: A case study with the Poker Flat Incoherent Scatter Radar, *J. Geophys. Res. Atmos.*, 115, D00N02, doi:10.1029/2010JD014042.

Okamoto, K., K. Sato, and H. Akiyoshi (2011), A study on the formation and trend of the Brewer - Dobson circulation, *J. Geophys. Res.*, 116, D10117, doi: 10.1029/2010JD014953.

Plougonven, R., and F. Zhang (2014), Internal gravity waves from atmospheric jets and fronts, *Rev. Geophys.*, 52, 33–76, doi:10.1002/2012RG000419.

Plumb, R. A. (2002), Stratospheric transport. *J. Meteorol. Soc Jpn.* Ser. II, 80(4B), pp. 793–809.

Polichtchouk, I., T. G. Shepherd, R. J. Hogan, and P. Bechtold (2018), Sensitivity of the Brewer–Dobson Circulation and Polar Vortex Variability to Parameterized Nonorographic Gravity Wave Drag in a High-Resolution Atmospheric Model. *J. Atmos. Sci.*, **75**, 1525–1543, https://doi.org/10.1175/JAS-D-17-0304.1.

Rienecker, M. M., M. J. Suarez, R. Gelaro, R. Todling, J. Bacmeister, E. Liu, M. G. Bosilovich, S.D. Schubert, L. Takacs, G. K. Kim, and S. Bloom (2011), MERRA: NASA's Modern-Era Retrospective Analysis for Research and Applications, *J. Clim*., 24, 3624–3648.

Sato, K. and M. Yoshiki (2008), Gravity wave generation around the polar vortex in the stratosphere revealed by 3-hourly radiosonde observations at Syowa Station, *J. Atmos. Sci.*, 65(12), 3719–3735, doi:10.1175/2008JAS2539.1.

Sato, K., S. Watanabe, Y. Kawatani, Y. Tomikawa, K. Miyazaki, and M. Takahashi (2009), On the origins of mesospheric gravity waves, *Geophys. Res. Lett.*, 36, L19801, doi:10.1029/2009GL039908.

Sato, K., S. Tateno, S. Watanabe, and Y. Kawatani (2012), Gravity wave characteristics in the Southern Hemisphere revealed by a high-resolution middle-atmosphere general

circulation model. *J. Atmos. Sci.*, 69, 1378–1396, https://doi.org/10.1175/JAS-D-11-0101.1.

Shibata, T., T. Fukuda, and M. Maeda (1986), Density fluctuations in the middle atmosphere over Fukuoka observed by an XeF Rayleigh lidar. *Geophys. Res. Lett.* 13.11, 1121–1124, https://doi.org/10.1029/GL013i011p01121.

Shibuya, R., K. Sato, Y. Tomikawa, M. Tsutsumi, and T. Sato (2015), A study of multiple tropopause structures caused by inertia gravity waves in the Antarctic. *J. Atmos. Sci.*, 72, 2109–2130, doi:10.11175/JAS-D-14-0228.1.

Sivakumar, V., P. B. Rao, and H. Bencherif (2006), Lidar observations of middle atmospheric gravity wave activity over a low-latitude site (Gadanki, 13.5° N, 79.2° E), *Ann. Geophys.*, 24(3), 823–834.

Stevens, M. H., L. E. Deaver, M. E. Hervig, J. M. Russell III, D. E. Siskind, P. E. Sheese, E. J. Llewellyn, R. L. Gattinger, J. Höffner, and B. T. Marshall (2012), Validation of upper mesospheric and lower thermospheric temperatures measured by the Solar Occultation for Ice Experiment, *J. Geophys. Res.*, 117, *D16304, doi:*10.1029/2012JD017689.

Suzuki, H., T. Nakamura, M. K. Ejiri, M. Abo, T. D. Kawahara, Y. Tomikawa, and M. Tsutsumi (2012), A Rayleigh-Raman lidar system for troposphere-mesosphere observations at Syowa station, Antarctica, Reviewed and Revised Papers Presented at the 26th International Laser Radar Conference (ILRC 2012), S9P-18.

Tsuda, T., and K. Hocke (2004), Application of GPS radio occultation data for studies of atmospheric waves in the middle atmosphere and ionosphere. *J. Meteorol. Soc. Jpn. Ser. II*, *82*(1B), 419–426.

Tsuda, T., M. Nishida, C. Rocken, and R.H. Ware (2000), A global morphology of gravity wave activity in the stratosphere revealed by the GPS occultation data (GPS/MET), *J. Geophys. Res.*, 105(D6), 7257–7273, doi:10.1029/1999JD901005.

Whiteway, J. A., and A. I. Carswell (1994), Rayleigh lidar observations of thermal structure and gravity wave activity in the high arctic during a stratospheric warming, *J. Atmos. Sci.*, 51, 3122–3136.

Whiteway, J. A., and A. I. Carswell (1995), Lidar observations of gravity wave activity in the upper stratosphere over Toronto, *J. Geophys. Res.*, 100(D7), 14113–14124, doi:10.1029/95JD00511.

Wilson, R., M. L. Chanin, and A. Hauchecorne (1991), Gravity waves in the middle atmosphere observed by Rayleigh lidar: 2. Climatology, *J. Geophys. Res.*, 96(D3), 5169–5183, doi:10.1029/90JD02610.

Wright, C. J., N. P. Hindley, A. C. Moss, D. C. Fritts, D. Janches and N. J. Mitchell (2015), Multi-instrument gravity-wave measurements over Tierra del Fuego and the Drake Passage-Part 1: Potential energies and vertical wavelengths from AIRS, COSMIC, HIRDLS, MLS-Aura, SAAMER, SABER, and radiosondes. *Atmos. Meas. Tech.*, *9*(3), 877, 6797–6876, doi:10.5194/amtd-8-6797-2015.

Yamashita, C., X. Chu, H. L. Liu, P. J. Espy, G. J. Nott, and W. Huang (2009), Stratospheric gravity wave characteristics and seasonal variations observed by lidar at the South Pole and Rothera, Antarctica, *J. Geophys. Res.*, 114, D12101, doi:10.1029/2008JD011472.

Yoshiki, M., and K. Sato (2000), A statistical study of gravity waves in the polar regions based on operational radiosonde data, *J. Geophys. Res.*, 105(D14), 17,995–18,011, doi:10.1029/2000JD900204.

Yoshiki, M., N. Kizu, and K. Sato (2004), Energy enhancements of gravity waves in the Antarctic lower stratosphere associated with variations in the polar vortex and tropospheric disturbances, *J. Geophys. Res.*, 109, D23104, doi:10.1029/2004JD004870.

Zhang, F. (2004), Generation of mesoscale gravity waves in the upper-tropospheric jet-front systems, *J. Atmos. Sci.*, 61, 440–457, doi:10.1175/1520-0469(2004)061<0440:GOMGWI>2.0.CO;2.

Zhao, J., X. Chu, C. Chen, X. Lu, W. Fong, Z. Yu, R. M. Jones, B. R. Roberts, and A. Dörnbrack (2017), Lidar observations of stratospheric gravity waves from 2011 to 2015 at McMurdo (77.84° S, 166.69° E), Antarctica: 1. Vertical wavelengths, periods, and frequency and vertical wave number spectra, *J. Geophys. Res.*, 122, 5041–5062, doi:10.1002/2016JD026368.

## Tables

| month / year | 2 | 3 | 4 | 5 | 6 | 7 | 8 | 9 | 10 | Total |
|---|---|---|---|---|---|---|---|---|---|---|
| 2011 | 0 | 0 | 0 | 6 | 1 | 12 | 12 | 12 | 9 | 52 |
| 2012 | 3 | 4 | 9 | 10 | 13 | 7 | 7 | 17 | 10 | 80 |
| 2013 | 0 | 7 | 12 | 11 | 10 | 13 | 5 | 10 | 7 | 75 |
| 2014 | 0 | 0 | 0 | 0 | 16 | 16 | 11 | 0 | 0 | 44 |
| 2015 | 0 | 0 | 10 | 11 | 20 | 8 | 14 | 11 | 13 | 87 |
| total | 3 | 11 | 31 | 38 | 60 | 56 | 49 | 50 | 39 | 338 |

Table 1. The number of RR lidar observation dates from May 2011 to October 2015.

**Figures**

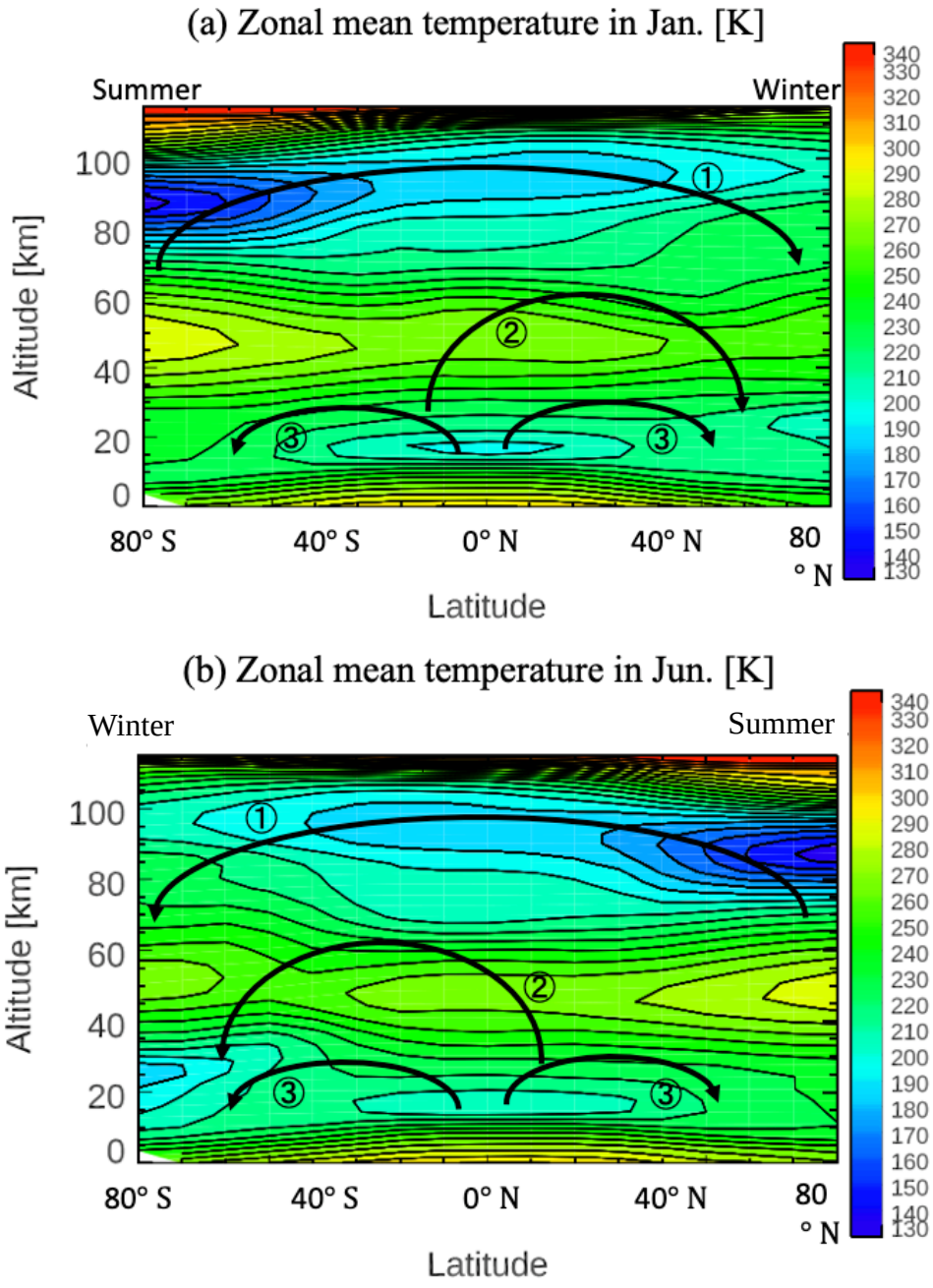


Figure 1.1 Latitude-Height sections of monthly- and zonal-mean temperature in (a) January, and (b) June from COSPAR International Reference Atmosphere 1986 (CIRA86) [*Fleming et al.*, 1990]. Contour intervals are 10 K. Black arrows indicate the meridional circulation in the middle atmosphere. ① Mesospheric circulation. ② Deep branch of the Brewer-Dobson circulation. ③ Shallow branch of the Brewer-Dobson circulation.

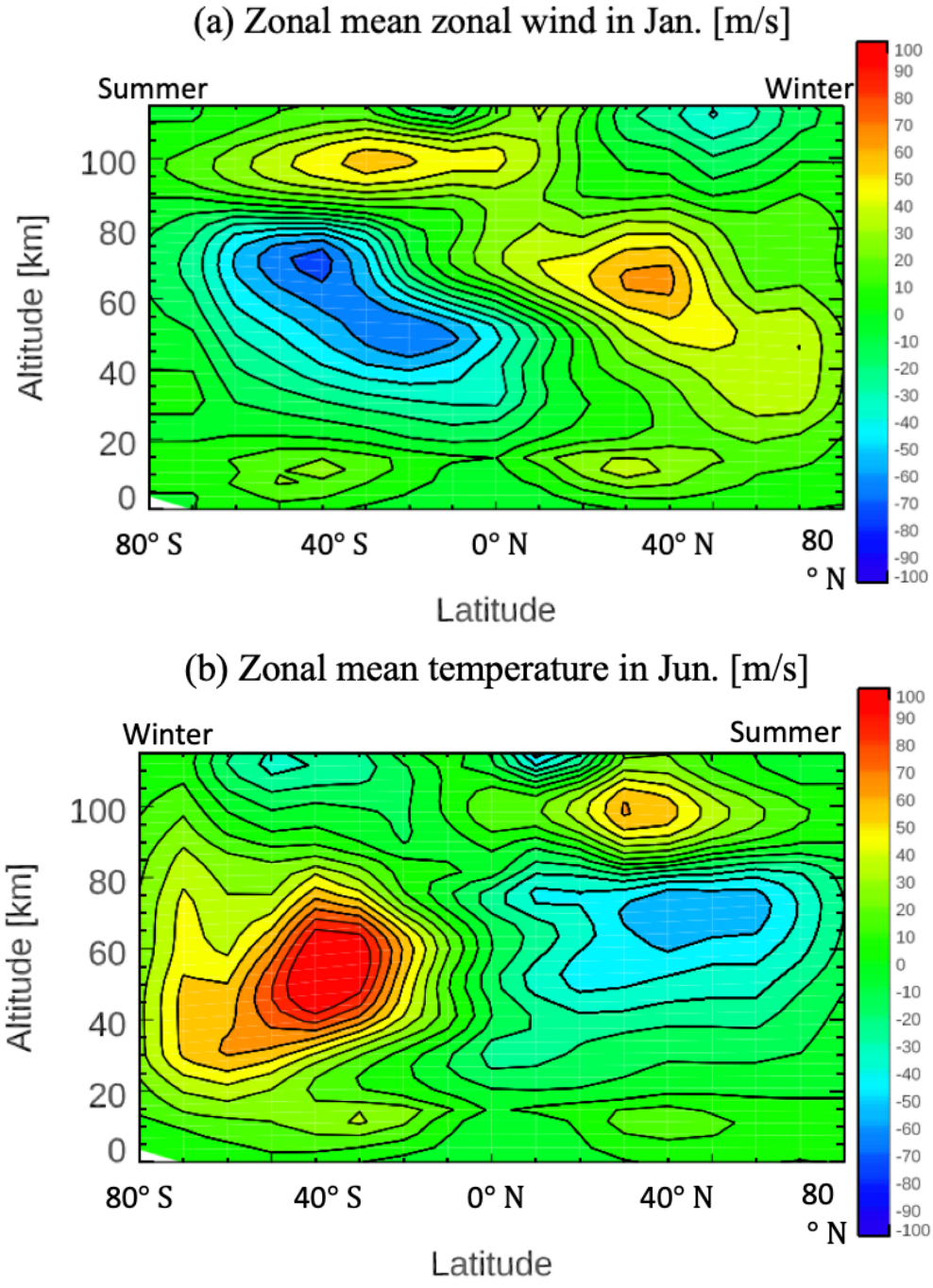


Figure 1.2 Figure 1.1 Latitude-Height sections of monthly- and zonal-mean zonal wind in (a) January, and (b) June from COSPAR International Reference Atmosphere 1986 (CIRA86) [*Fleming et al.*, 1990]. Contour intervals are 10 m/s.

–1989 at Haute–Provence

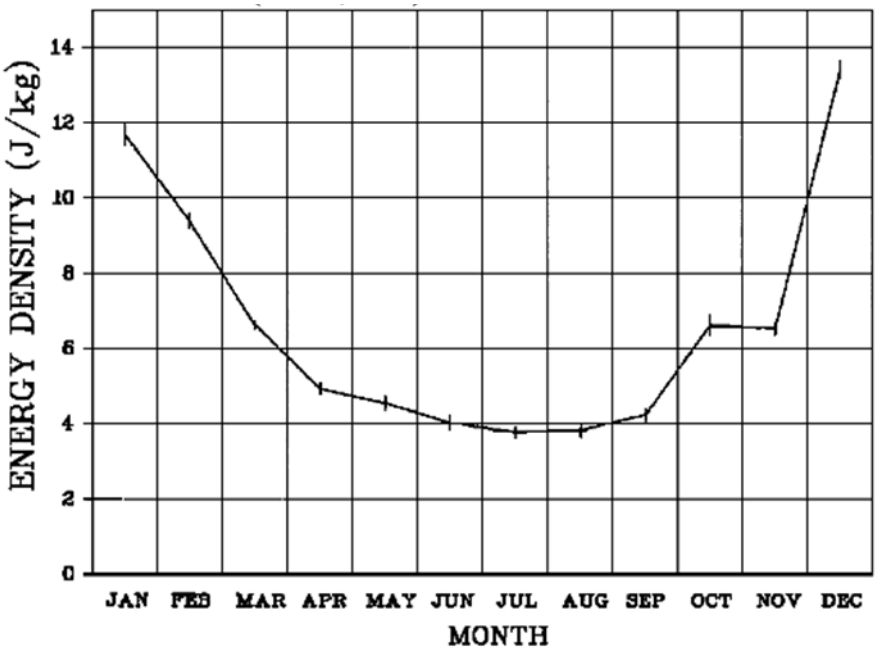


Figure 2.1 Monthly mean potential energy of AGW observed by the Rayleigh lidar at Haute-Provence [*Wilson et al*., 1991]

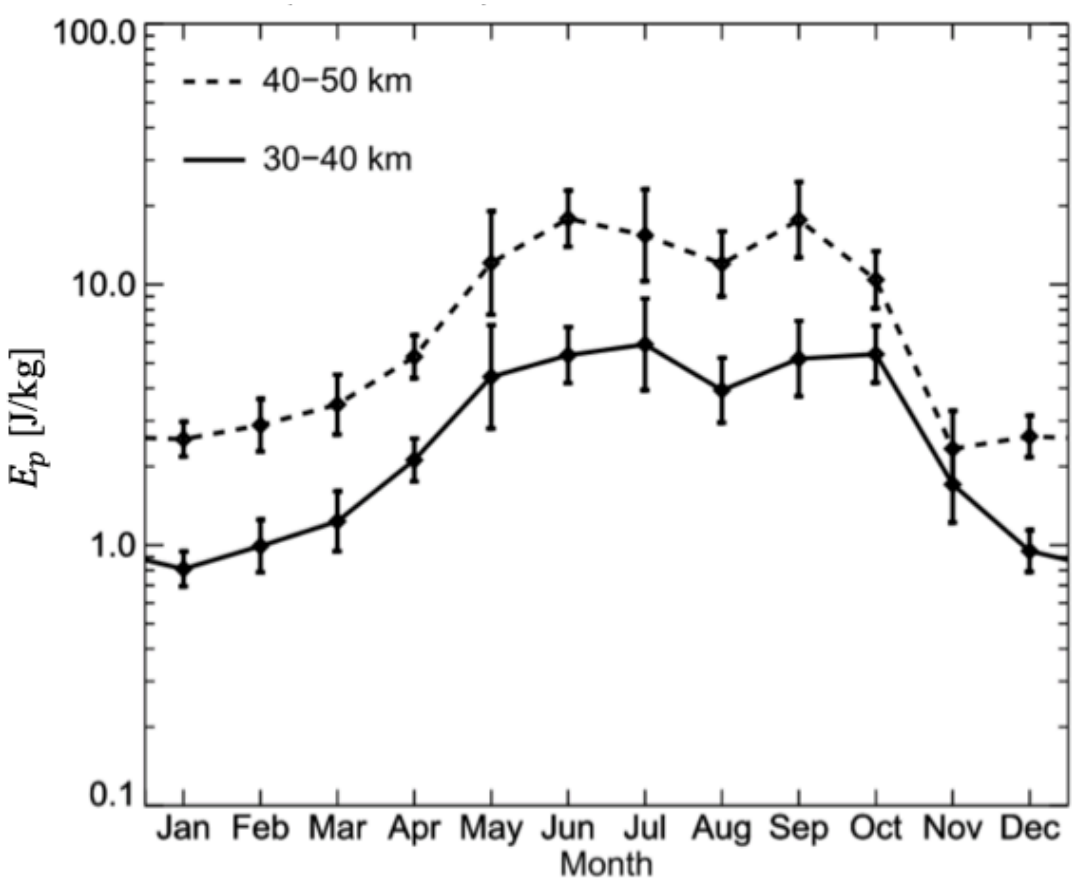


Figure 2.2 Monthly mean potential energy of AGW observed by the Rayleigh lidar at 30–40 km (solid) and 40–50 km (dashed) over Davis [*Kaifler et al.*, 2015]. Bars represent standard deviations.

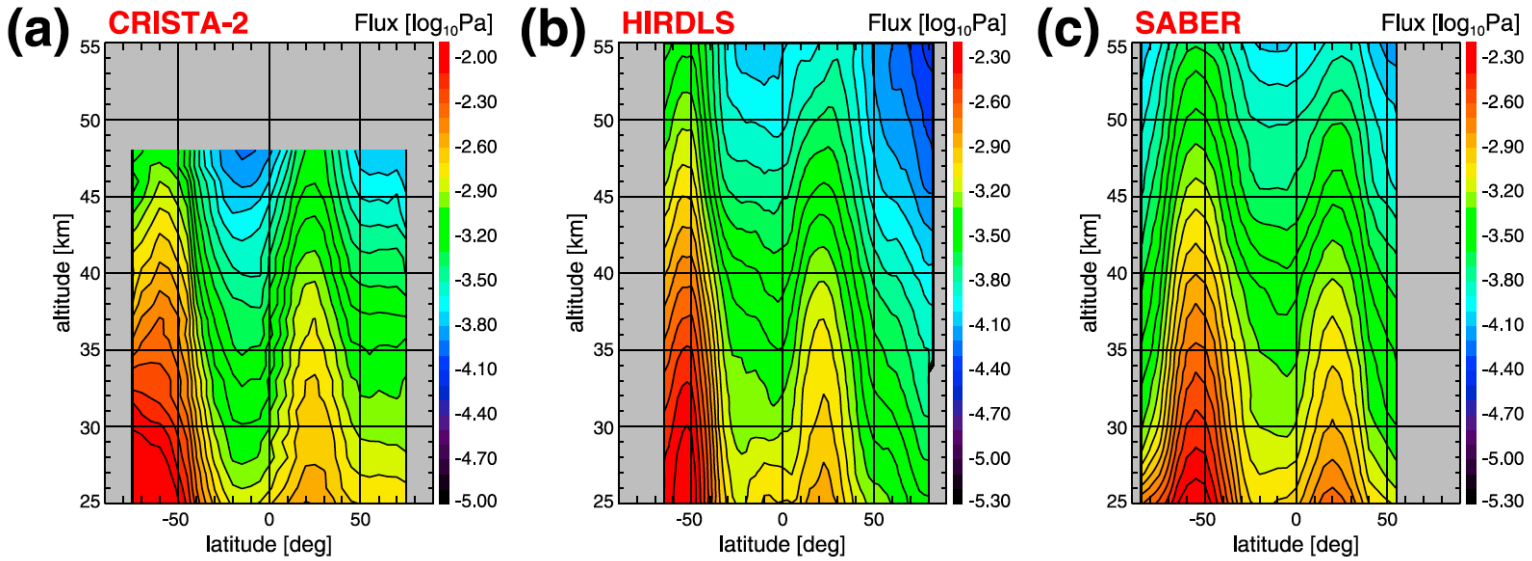


Figure 2.3 Latitude-altitude sections of the absolute momentum flux for (a) CRISTA-2, (b) HIRDLS and (c) SABER in August 2006.

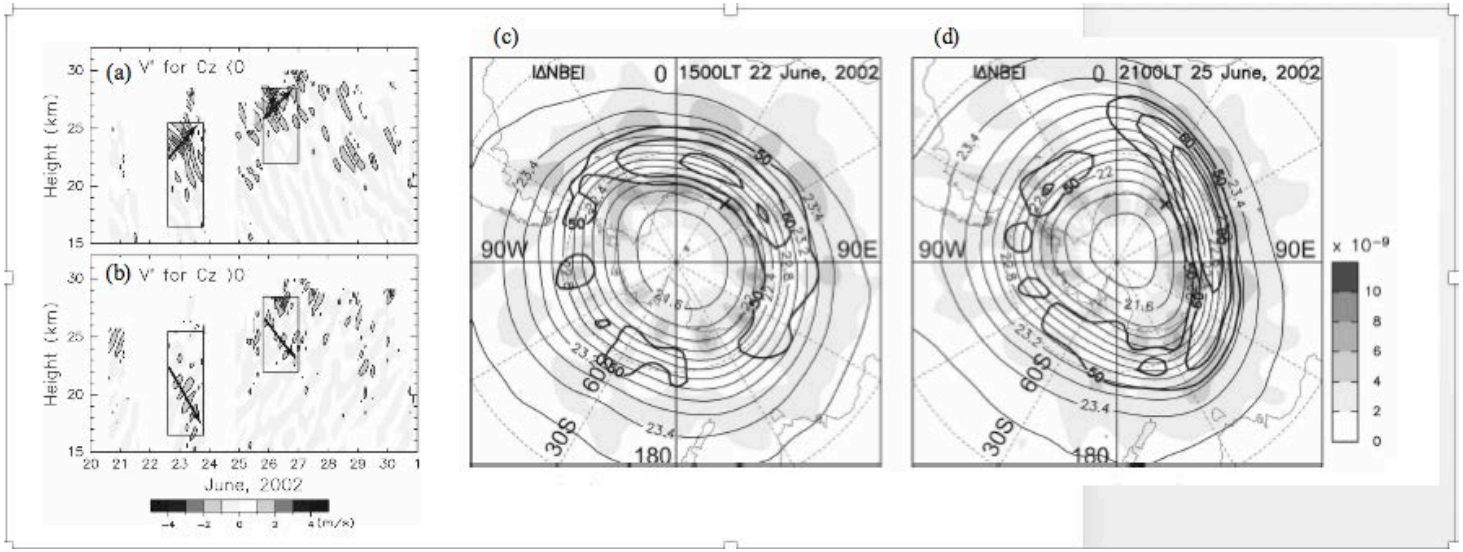


Figure 2.4 Time-altitude sections of meridional wind fluctuations of AGW with (a) upward and (b) downward propagation. The rectangles denote the regions for strong wave packets. Arrows indicate the propagation direction of AGW. Polar stereograms of the absolute value of ΔNBE at 30 hPa at (c) 15 LST June 22, and (d) 21 LST June 25, 2002, derived from NCEP-NCAR reanalysis data. Thin contours indicate geopotential heights (in km) with an interval of 300 m and thick contours indicate the absolute value of horizontal winds (50, 60, and 70 m $s^{-1}$). Cross indicates Syowa location [*Sato and Yoshiki*, 2008].


Figure 3.1 Syowa Rayleigh/Raman lidar.

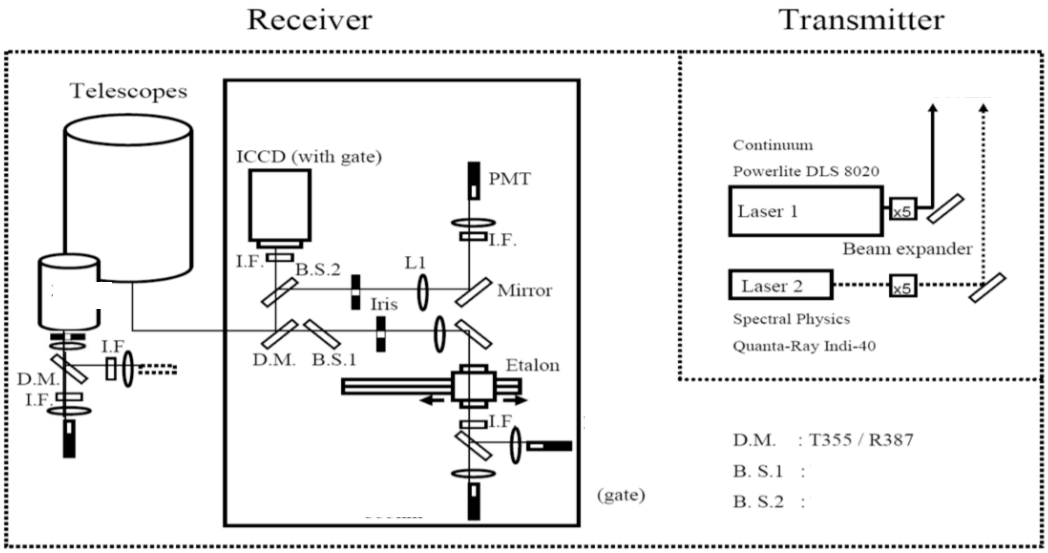


Figure 3.2 Block diagram of the Rayleigh/Raman lidar at Syowa Station.

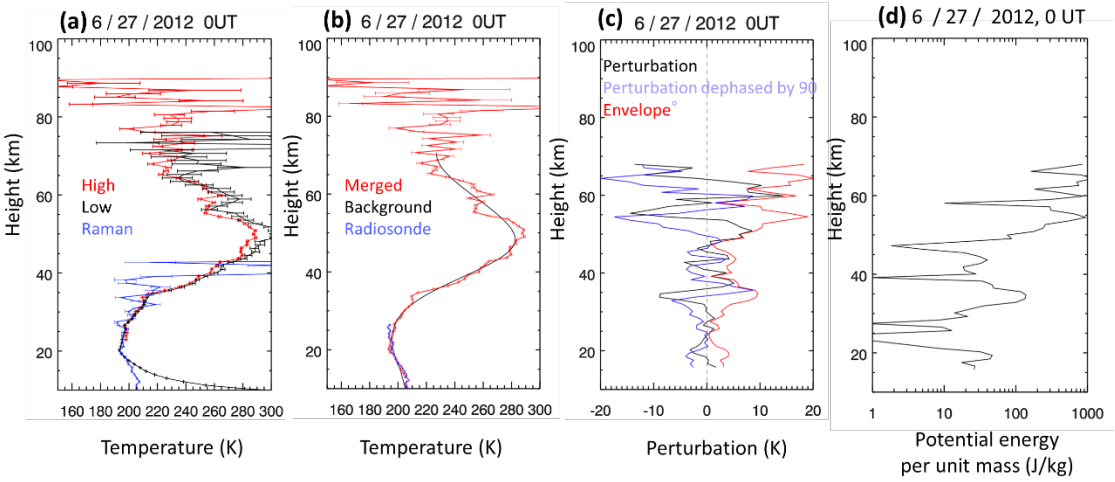


Figure 3.3 (a) Temperature profiles observed using the Rayleigh high (red), Rayleigh low (black), and Raman channels (blue) at 23:30–24:30 UT on June 27, 2012 at Syowa Station. The horizontal bars indicate standard deviation errors caused by shot noise. (b) Merged temperature (red) and estimated background temperature (black) profiles obtained by the lidar. The blue line indicates a temperature profile obtained by the concurrent radiosonde observation. (c) Temperature perturbation (black), its Hilbert transform (blue), and the envelope (red). (d) Instantaneous $E_p$ profile (see the text for details).

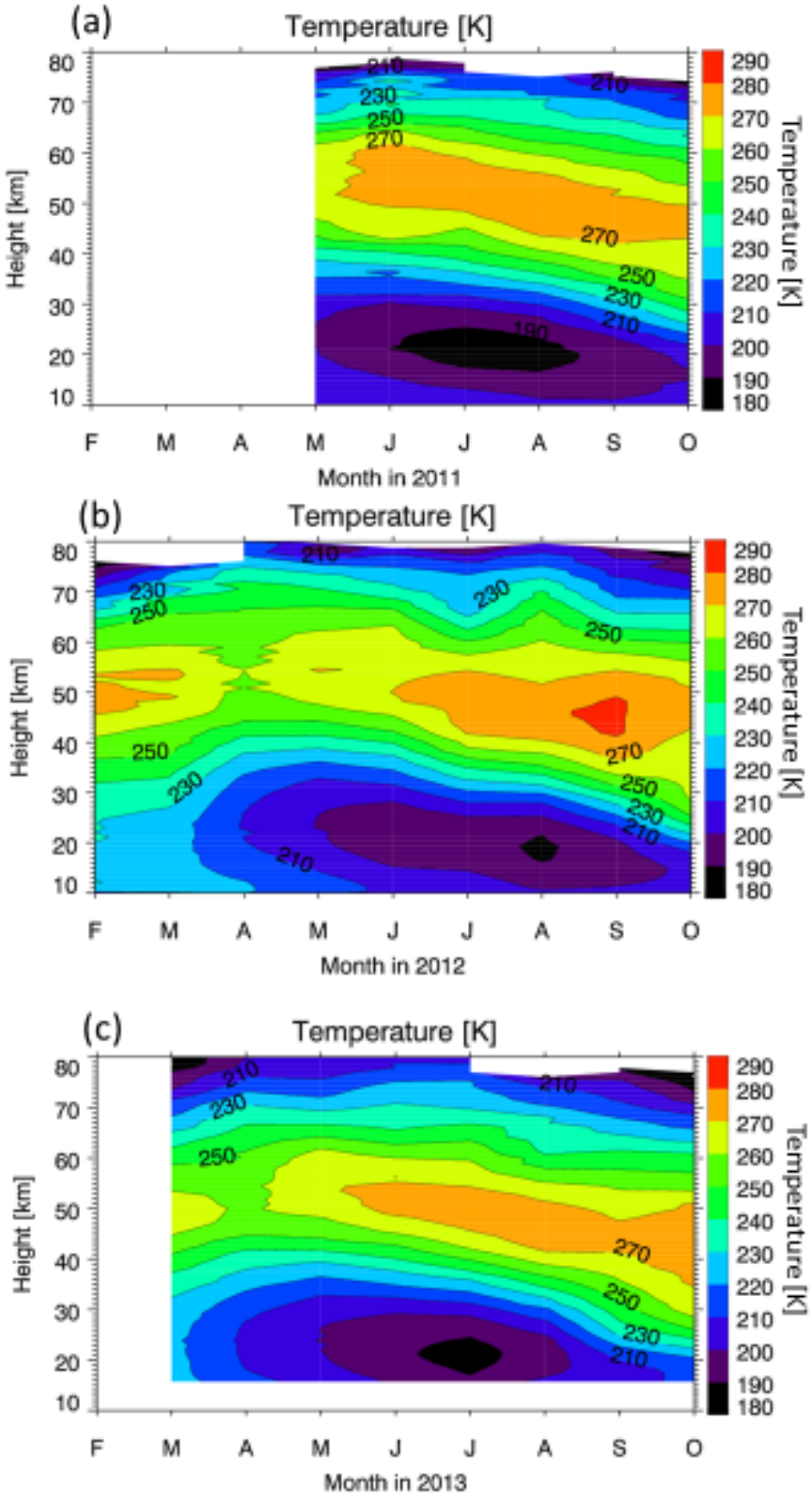


Figure 4.1 Time–altitude sections of monthly mean temperature acquired using RR lidar observations in (a) 2011, (b) 2012, and (c) 2013.

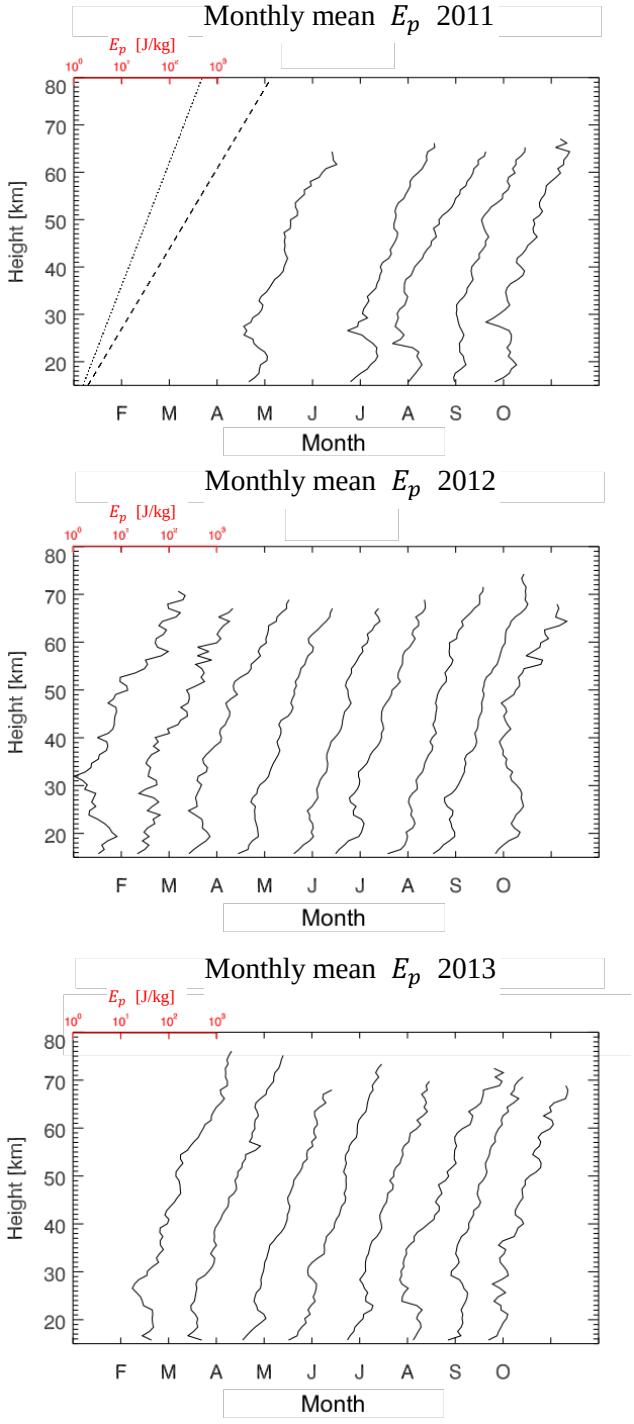


Figure 4.2 Time series of monthly mean $E_p$ profiles in (a) 2011, (b) 2012, and (c) 2013. The profiles are shifted by $10^1$ intervals for each month. The dashed and dotted lines indicate the slope of the density scale height ($H$ = 7.3 km, $H$ is calculated from mean temperature between 30 and 70 km over 3 years) and the slope of the mean $E_p$ scale height, respectively.

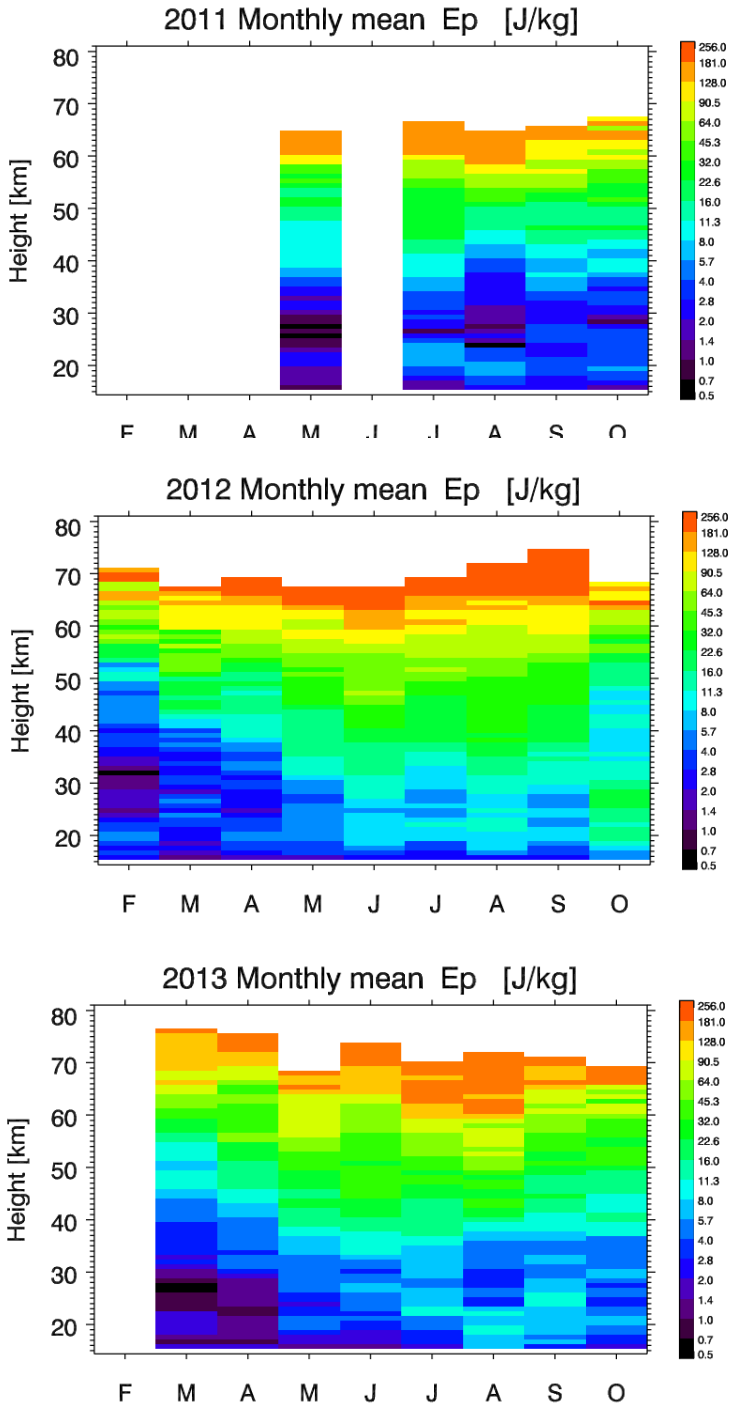


Figure 4.3. Time–altitude sections of monthly mean $E_p$ in (a) 2011, (b) 2012, and (c) 2013. The $E_p$ in June 2011 has been removed, owing to insufficient observation time.

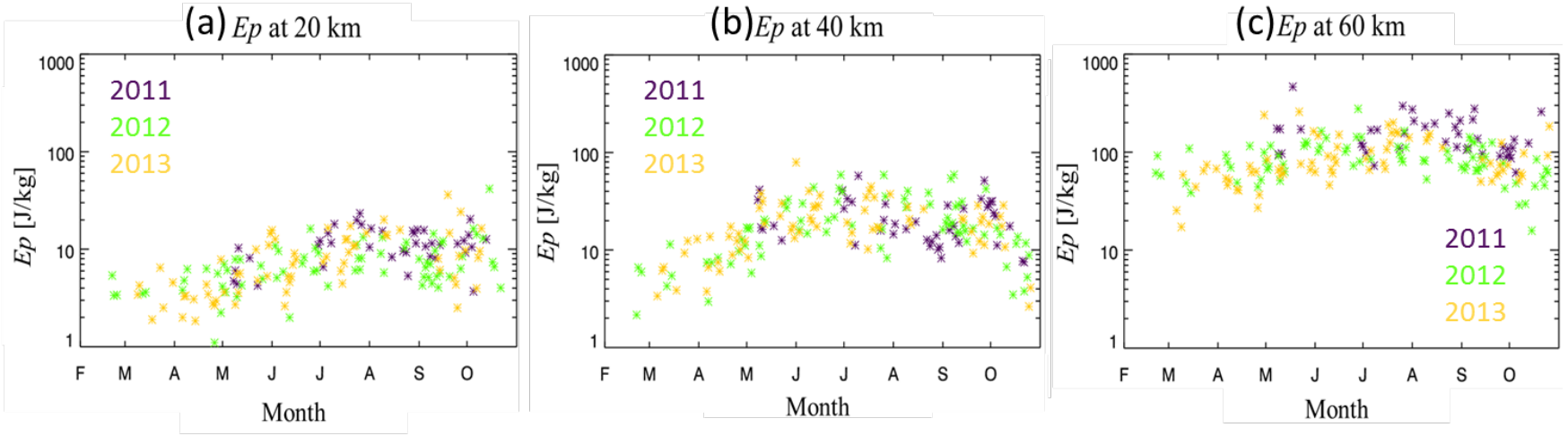


Figure 4.4 Seasonal variations of nightly mean $E_p$ at (a) 20 km, (b) 40 km, and (c) 60 km. The blue, yellow, and green asterisks indicate the $E_p$ values in 2011, 2012, and 2013, respectively.

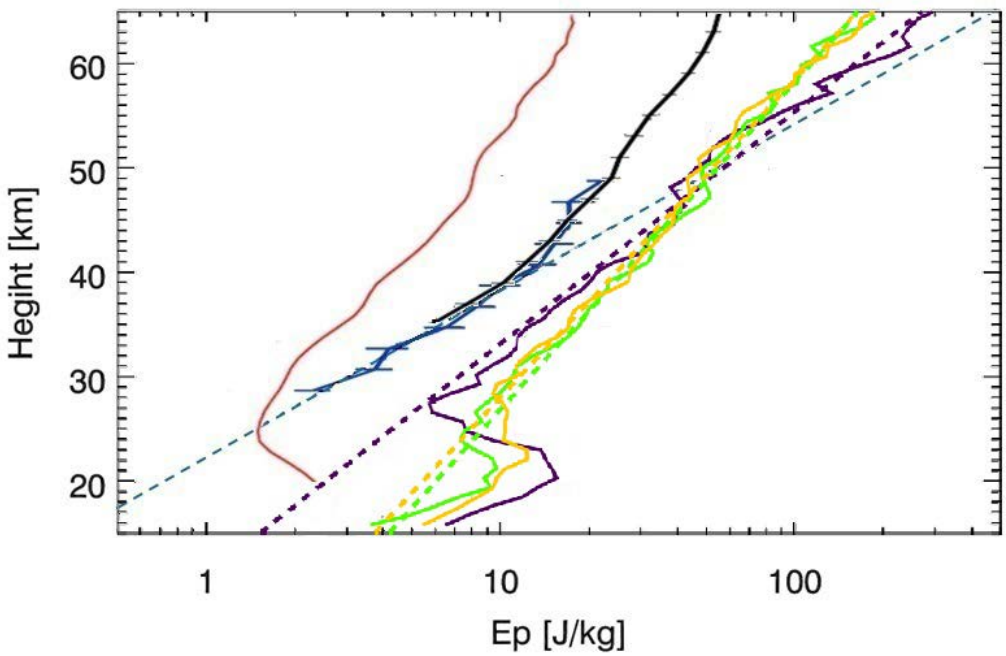


Figure 4.5 Comparison of $E_p$ profiles. The red line is the mean $E_p$ profile in winter over 63–78° S during 2007–2013 estimated from temperatures observed by SOFIE/AIM [*Liu et al.*, 2014]. The black and blue lines are the mean $E_p$ profiles over Davis during 2007–2008 and 2011, respectively [*Alexander et al.*, 2011; *Kaifler et al.*, 2015]. The blue dashed line indicates the slope of the $E_p$ between 29 and 40 km altitude [*Kaifler et al.*, 2015]. The green, purple, and yellow lines are the mean $E_p$ profiles in winter over Syowa during 2011, 2012, and 2013, respectively. The green, purple, and yellow dashed lines indicate their corresponding linear fittings.

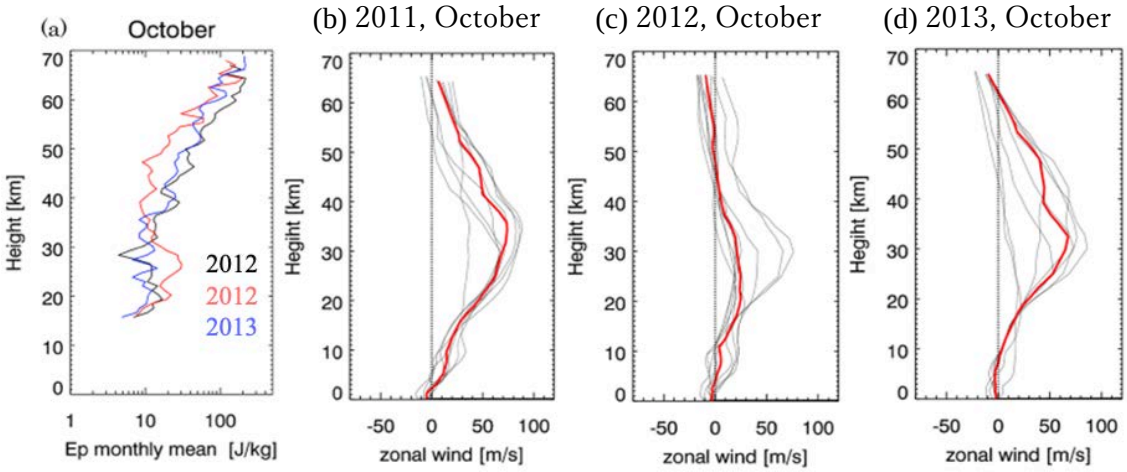


Figure 4.6 (a) Monthly mean $E_p$ in October of 2011 (black), 2012 (red), and 2013 (blue). (b–d) Nightly-mean zonal winds from MERRA over Syowa Station on the observation dates in (b) 2011, (c) 2012, and (d) 2013. The red lines represent the median profile of October for each year.

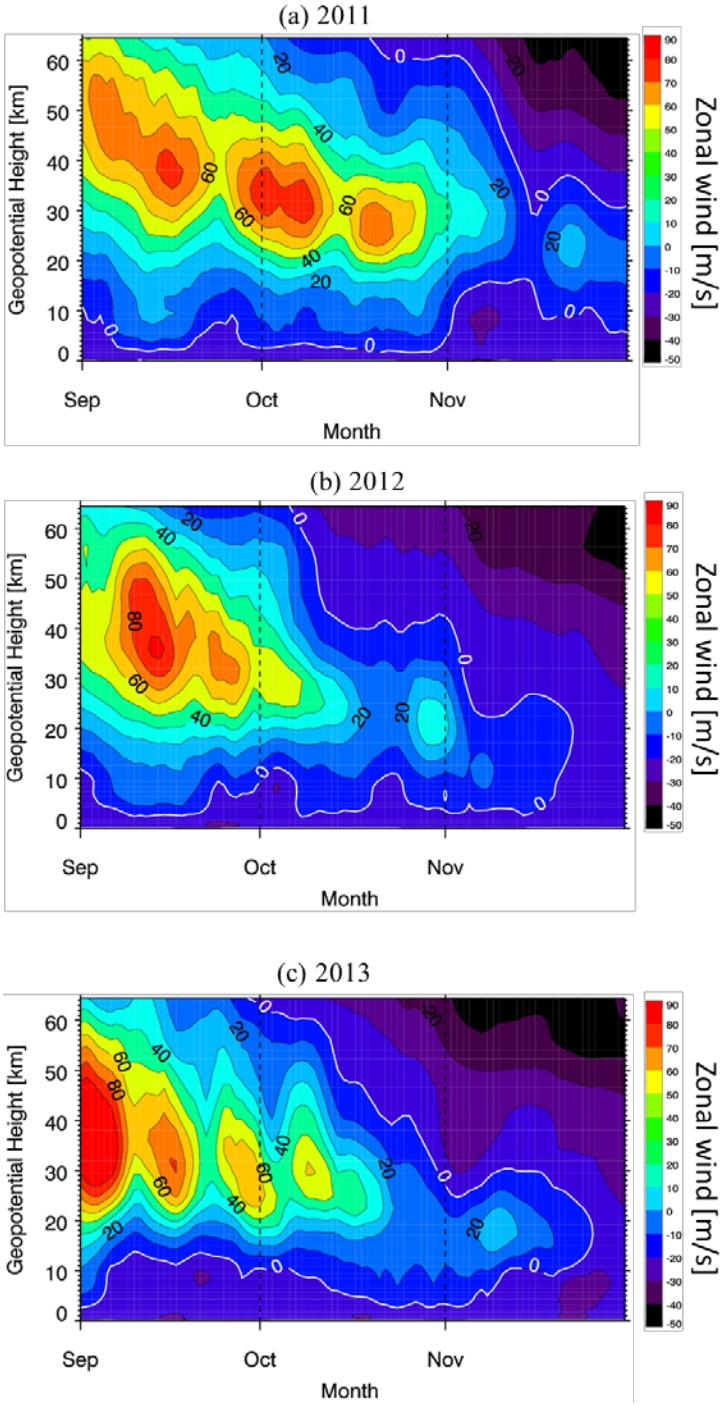


Figure 4.7 Time–height sections of weekly running averaged zonal wind obtained from MERRA over Syowa from September to November in 2011 (a), 2012 (b), and 2013 (c). The *y*-axis indicates the mean geopotential height in September to November. The dashed lines represent the first day of each month. The thick white lines indicate 0 m $s^{-1}$.

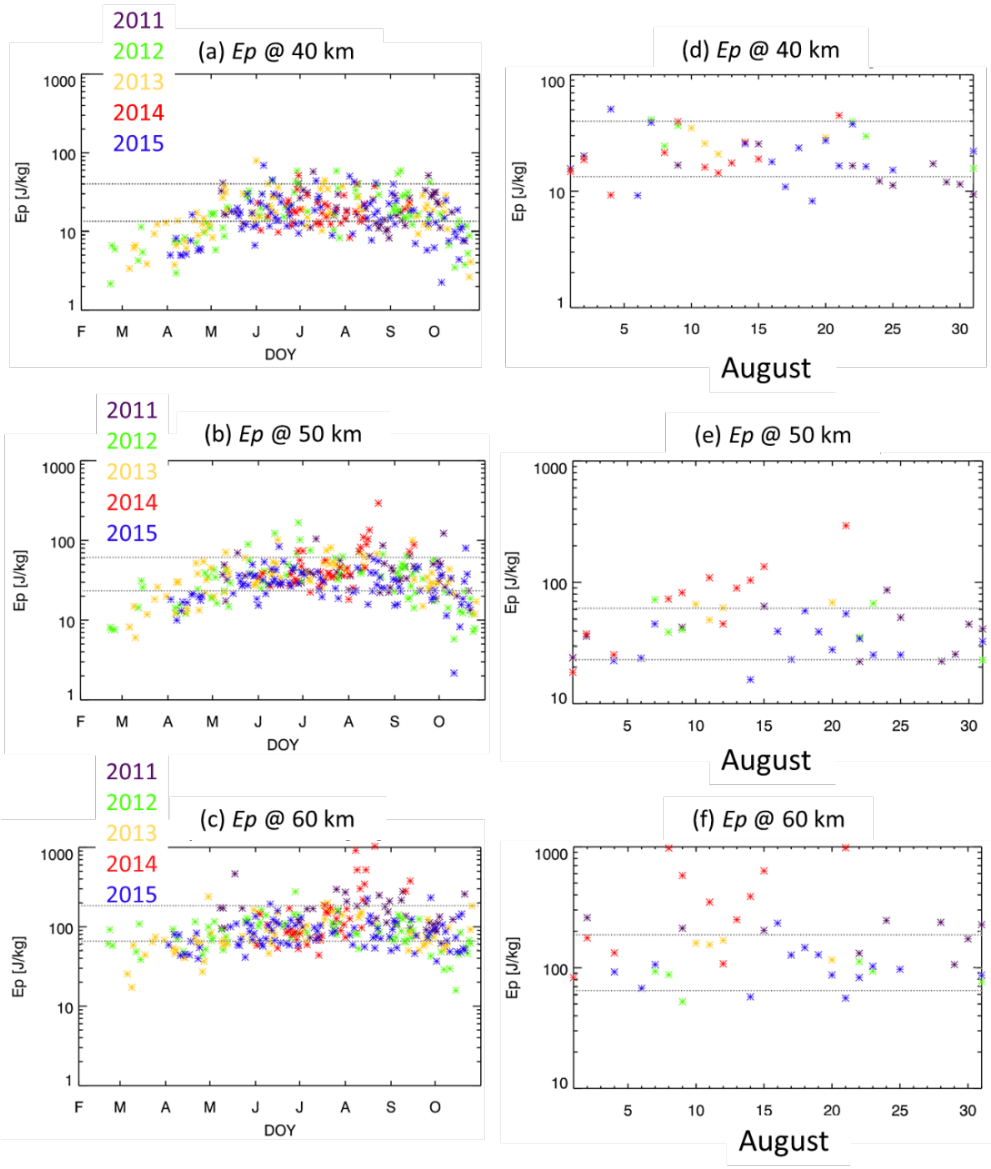


Figure 5.1 Day-to-day variations of the nightly mean $E_p$ at (a) 40, (b) 50, and (c) 60 km. The purple, green, yellow, red, and blue asterisks indicate the $E_p$ values in 2011, 2012, 2013, 2014, and 2015, respectively. The dashed lines indicate $[E_p]_{winter} \pm \sigma_{winter}$. The variations for August are enlarged at (d) 40, (e) 50, and (f) 60 km.

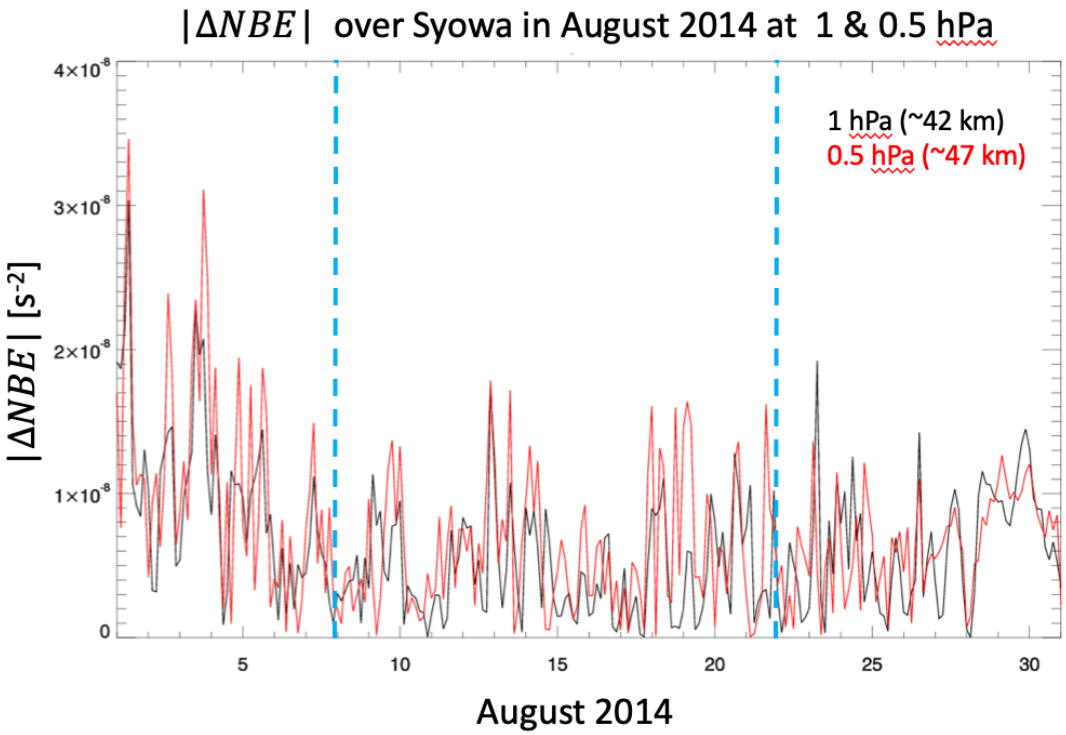


Figure 5.2 The residual of the nonlinear balance equation ($|\Delta NBE|$), acquired from MERRA, at 1 hPa (black line) and 0.5 hPa (red line) in August 2014. The blue lines indicate the enhancement period.

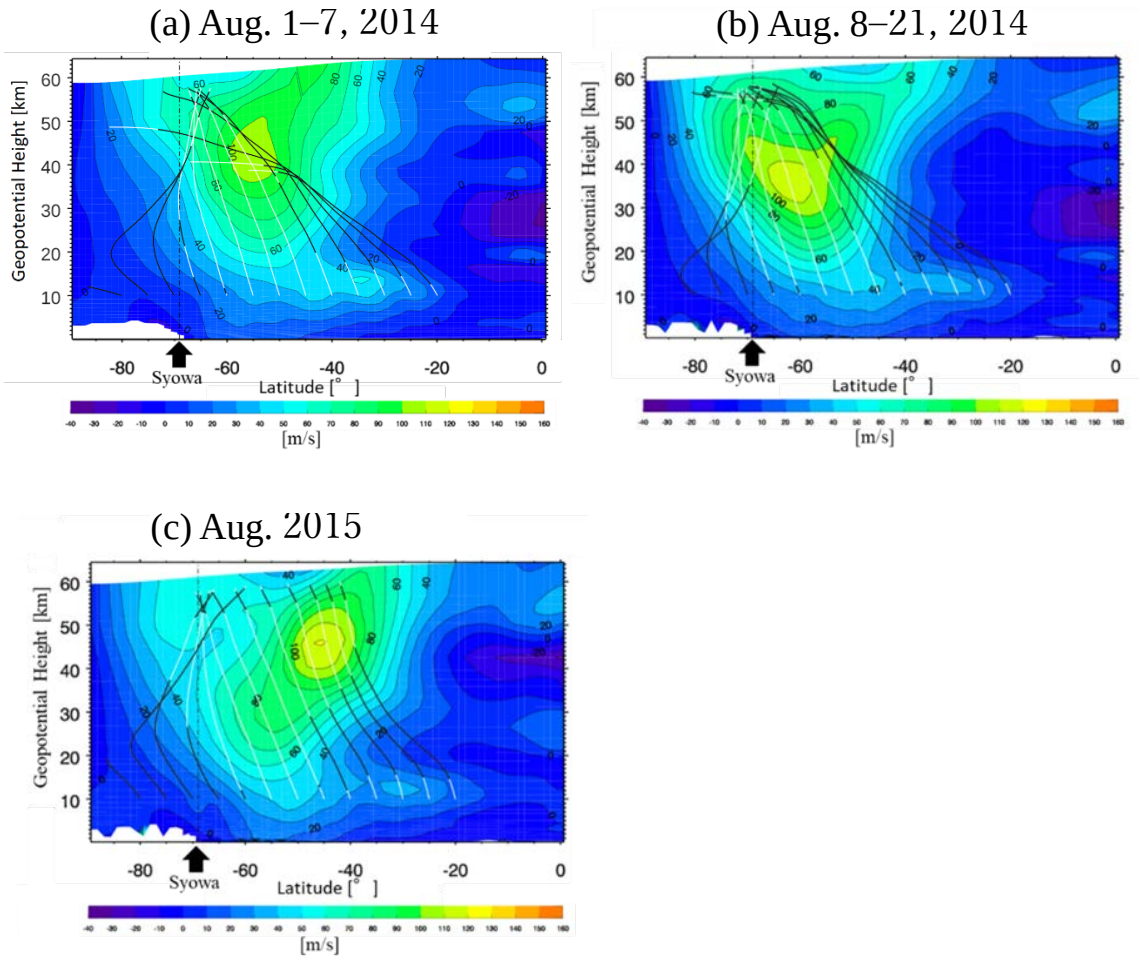


Figure 5.3 Latitude-altitude sections of the nightly mean zonal wind acquired from MERRA in (a) August 1–7, 2014, (b) August 8–21, 2014, and (c) August 2015. Black and white lines indicate rays of the AGWs whose vertical wavelengths can and cannot be observed by the RR lidar, respectively. Arrows indicate the latitudes of Syowa.

Meridional wind during Aug. 8–22, over Syowa

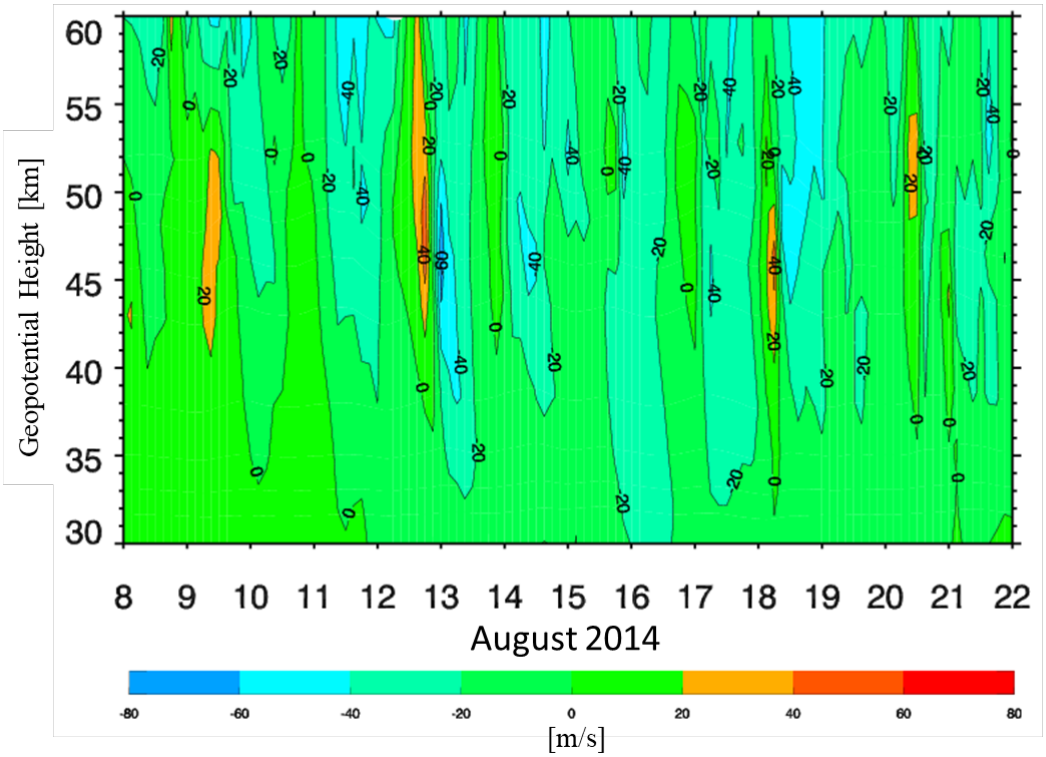


Figure 5.4 Time-altitude section of meridional wind at Syowa acquired from MERRA.

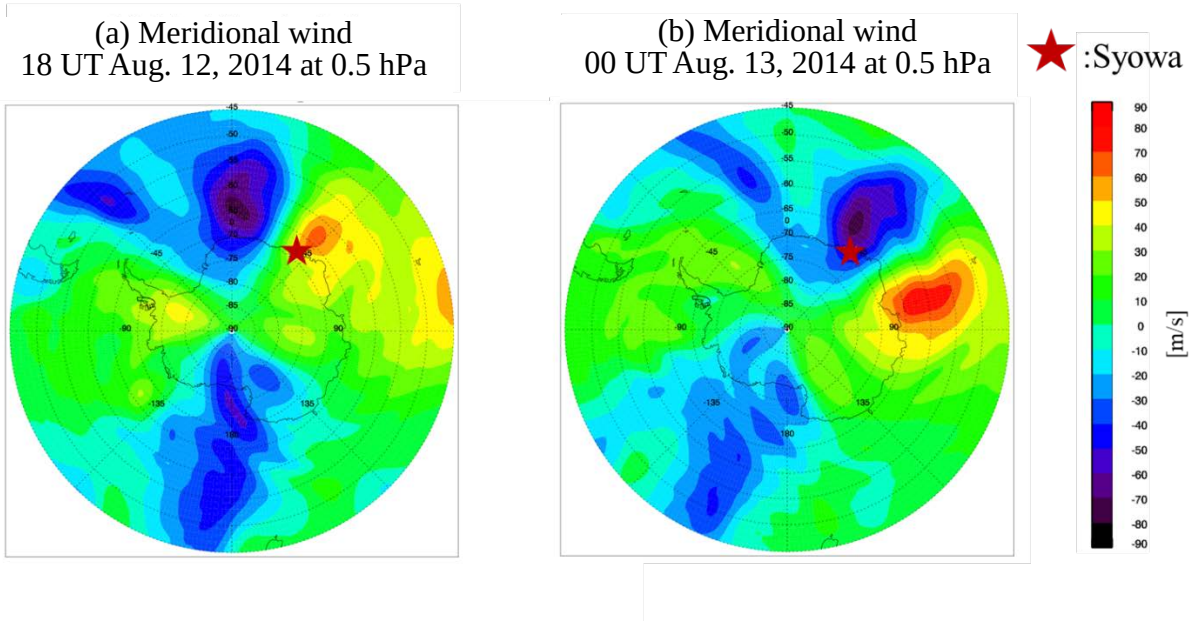


Figure 5.5 Meridional wind fields acquired from MERRA at 0.5 hPa at (a) 18 UT August 12 and (b) 00 UT August 13, 2014. The red star represents the location of Syowa Station.